UNIVERSITY OF CALIFORNIA
RIVERSIDE

Electrical and Thermal Characterization of Low – Dimensional Materials and Devices

A Dissertation submitted in partial satisfaction
of the requirements for the degree of

Doctor of Philosophy

in

Materials Science and Engineering

by

Ruben A. Salgado

June 2019

Dissertation Committee:
Dr. Alexander A. Balandin, Chairperson
Dr. Roger Lake
Dr. Alexander Khitun

The Dissertation of Ruben A. Salgado is approved:

_____

_____

_____

Committee Chairperson

University of California, Riverside

Acknowledgements

I would like to grant my sincerest gratitude to several individuals I had the pleasure of meeting during my graduate studies. These individuals have helped me grow on a professional and personal level. I would first like to thank my advisor, Dr. Alexander A. Balandin, who I first met as an undergraduate student many years ago. His enthusiasm along with his unmatched intellect and insight still inspire me today. I would like to thank him for granting me the opportunity to conduct world class research under his endearing guidance and supervision. I can only hope to attain his level of expertise and candor when approaching complex problems. I would also like to thank Dr. Roger Lake and Dr. Alexander Khitun for serving on my dissertation committee. I am grateful for meeting Dr. Denis Nika, Dr. Sergey Rumyantsev, and Dr. Monica Lacerda who were all visiting researchers during my studies. They provided an exemplary level of understanding in material physics which helped many of us reach breakthroughs in our research. I thank Dr. Elena V. Schevchenko, Argonne National Laboratory, who provided synthesized carbon – nanotube – based cathodes and performed all electrochemical tests, SEM imaging and SAXs morphology studies. I also thank Tina T. Salguero from the University of Georgia, Athens who provided 1*T* – TaS_2 bulk crystals and performed various crystal characterization measurements.

I would like to express my gratitude to my fellow lab mates from the Nano Device Laboratory (NDL) and the center for Phonon Optimized Engineered Materials (POEM), as well as friends outside my research group. I would personally like to thank Pradyumna

Goli for being the first member to welcome me into these groups with open arms. His guidance during my undergraduate studies immensely helped me as a graduate student. I thank past NDL and POEM members which include Aditya Dhar, Stanislav Legedza, Dr. Zhong Yan, Dr. Richard Gulotty, Dr. Hoda Malekpour, Dr. Maxim Stolyarov, Dr. Mahesh Neupane, Dr. Guanxiong Liu, Dr. Ece Coleman Aytan, Maedeh Taheri, Dr. Jackie Renteria, Dr. Rameez Samnakay, Dr. Chenglong Jiang, Dr. Mohammed Saadah, and Dr. Selcuk Temiz. I would also like to thank the current members of NDL and POEM which include Tammy Huang, Zahra Barani, Amirmahdi Mohammadzadeh, Jacob Lewis, Subhajit Ghosh, Adane Geremew, Sahar Naghibi, Barath Mahadevan, and Dr. Fariborz Kargar. They provided a research environment rich in creative discussion and collaborative spirit. During my time in NDL, I mentored several undergraduate students. I would like to thank them for giving me the opportunity to mentor and guide them throughout their undergraduate studies. These students include Edward Hernandez, Robert Hernandez, Regina Huang and Dineth Gamalath. I would like to thank the National Science Foundation (NSF) who sponsored my work through grants ECCS 1549942, CMMI 1404967 and the EFRI 2–DARE project: Novel Switching Phenomena in Atomic MX_2 Heterostructures for Multifunctional Applications (NSF EFRI–1433395).

Finally, I would like to give my profound thanks to my family who supported me throughout my studies. My special thanks go to my mother Nora Salgado, my sister Angela Cervantes, and my brother–in–law Robert Cervantes. I also thank my older two brothers Isaac Saavedra and Danilo Salgado. I would like to thank my beautiful and soon to be fiancé Zaira Alibai. Her support toward the end of my PhD studies has been immeasurable

Parts of this dissertation were written based on or reprinted from previously published material as it is presented in the following journals:

- E. Lee, R.A. Salgado, B. Lee, A. V. Sumant, T. Rajh, C. Johnson, A.A. Balandin, E. V. Shevchenko, “Design of lithium cobalt oxide electrodes with high thermal conductivity and electrochemical performance using carbon nanotubes and diamond particles,” Carbon, Vol. 129, pp. 702–710, 2018. Reprinted with permission from Copyright © 2018 Elsevier.
- R. Salgado, A. Mohammadzadeh, F. Kargar, A. Geremew, C. Huang, M. A. Bloodgood, S. Rumyantsev, T. T. Salguero, A. A. Balandin “Low – frequency noise spectroscopy of charge – density – wave phase transitions in vertical quasi – 2D 1*T* – TaS_2 devices,” Appl. Phys. Express, vol. 12, 037001, 2019. Reprinted with permission from Copyright © 2019 The Japan Society of Applied Physics.

Dedicated

To my Mother

ABSTRACT OF THE DISSERTATION

Electrical and Thermal Characterization of Low – Dimensional Materials and Devices

by

Ruben A. Salgado

Doctor of Philosophy, Graduate Program in Materials Science and Engineering
University of California, Riverside, June 2019
Dr. Alexander A. Balandin, Chairperson

Low-dimensional materials such as quasi-one-dimensional carbon nanotubes and quasi-two-dimensional transition metal dichalcogenides reveal interesting properties, which have potential for future device applications. In some cases, the attractive feature of low-dimensional materials is their heat conduction capabilities, in other cases-it is the unusual electronic conduction and switching phenomena. In this dissertation research, I investigate (i) the thermal characteristics of carbon nanotubes incorporated in a battery electrode; and (ii) the electronic characteristics of quasi-two-dimensional 1*T*-TaS_2 material system and devices based on these systems. The selected material systems and different properties demonstrate a wide range of possibilities of the device applications for the low-dimensional materials. In the first part of this dissertation work, I describe the effects of the incorporation of carbon nanotubes, known for their high thermal conductivity, into Li-ion battery electrodes. It was demonstrated that the in-plane thermal conductivity of the composite electrodes with incorporated carbon nanotubes is as large as ~206 W/mK. This value exceeds the thermal conductivity of conventional laminated electrodes by about three orders of magnitude. The cross-plane thermal conductivity of the carbon-nanotube-based

electrodes is in the same range as thermal conductivity values of conventional laminated electrodes. The electrodes with carbon nanotubes revealed a superior electrochemical performance and stability. The results of this research demonstrated that the incorporation of highly thermally conductive low-dimensional materials can substantially improve the thermal properties of the battery electrodes without degrading their electrochemical performance. In the second part of this dissertation research, I report results of the investigation of current-voltage characteristics and low-frequency current fluctuations in vertical 1*T*-TaS_2 charge-density-wave devices. The electron transport, perpendicular to the atomic planes, was studied in the temperature range below T= 180 K, which is a known transition temperature to the commensurate charge-density-wave regime. The resistivity of the vertical 1*T*-TaS_2 devices reveal an intriguing abrupt change below 100 K. The low-frequency noise spectra suggest a presence of an additional "hidden" phase transition at this point. The obtained results confirmed the potential use of low-frequency noise spectroscopy for the investigation of electron transport and switching phenomena in low-dimensional materials.

Table of Contents

List of Figures

List of Tables

Chapter 1

1 Introduction

The first observation of low – dimensional materials was made during the early 20th century by the eventual 1925 Nobel Prize Laureate in Chemistry, Richard Zsigmondy [1]. In 1914 he published his work on the use of an ultra – microscope that utilizes the dark field method to observe particles with size dimensions much smaller than the wavelength of light [1]. Zsigmondy was able to observe a colloidal suspension of gold particles with dimensions 10,000 times smaller than that of a strand of human hair. He was also the first to coin the term nanometer (nm), as he determined it to be six order of magnitude less than a millimeter. Currently, materials with low – dimensionality are described as having at least one dimension less than 100 nm, granting them physical properties between its bulk form and constituent individual atoms. Materials constrained to under 100 nm in two directions are known as one – dimensional (1D) materials and can be visualized as "nano" – wires or "nano" – tubes, while materials constrained in one direction are labeled two – dimensional materials (2D) and exist in the form of "nano" – ribbons or "nano" – sheets. These materials have shown exotic properties such as high carrier mobility [2], high current density [3], resistive switching [4], radiation hardness [5], electromagnetic shielding [6] and high thermal conductivity [7]. Because of their outstanding intrinsic properties, low – dimensional materials are being studied in many different fields such as energy storage and

generation [8, 9], high – speed electronics [10], optical devices [11], chemical sensors [12, 13], hybrid materials [14, 15], and DNA sequencing [16, 17].

In this work, the electrical and thermal characteristics of both 1D carbon nanotubes and 2D 1T – TaS_2 materials are investigated. In section 1.1, the heat transport optimization of current lithium ion battery cells with the implementation of highly thermally conductive carbon nanotubes is discussed. In section 1.2, a phenomenon known as the charge density wave effect is discussed along with how materials which show this effect can be used to fabricate a new paradigm of advanced electronics which will compliment silicon – based devices. Finally, the overview of my dissertation is presented in section 1.3.

1.1 Thermal Management of Lithium Ion Batteries

Over the past decades, the global energy sector has undergone a transformation which has taken it from fossil fuels to a new focus on renewable energy [18, 19]. This transformation has placed Lithium – ion (Li – ion) batteries on the forefront of the future of the global energy market. Recently, there has been an expanded and ever–growing usage of Li – ion batteries for drones, electric vehicles and grid energy storage [20]. Li – ion batteries are attractive because of their low weight and high power density which make them attractive for applications in many fields including the automotive and aerospace industries [21]. Recent research on cathode materials has led to an improvement in the overall design of light weight, high power density Li – ion batteries [22]. Previously, there had been insufficient attention given to the improvement of the overall safety of Li – ion batteries.

Although Li – ion batteries convert stored chemical potential into electric energy, a considerate amount of energy is lost through ohmic heating. This results from the current flowing through the internal resistance of the battery during charging and discharging [23–32]. The chemical reactions which take place during the normal operation of Li – ion batteries also contribute to an internal buildup of heat. Overheating issues in Li – ion batteries eventually lead to thermal runaway and catastrophic failure. Over the last ten years, there have been several publicized Li – ion related fires, most of them involving electrical vehicles and two of them aircrafts [33–36]. These incidents highlight the importance of proper thermal management in Li – ion batteries.

The current thermal management system of Li – ion battery packs consists of either active cooling via liquid or air convective heat transfer media [37–42], or passive cooling using phase change material (PCMs) or an aluminum heatsink [43–48]. Active cooling is used in industrial scale applications in the aerospace and automotive fields, while passive cooling is used in small scale applications such as small electronic vehicles. Both active and passive cooling have drawbacks that must be addressed. Active cooling systems are complex, costly and bulky, while passive cooling systems exploit PCM's heat absorbing properties to transfer heat away from batteries out to the surrounding environment. The intrinsic low thermal conductivity of PCMs results in a poor heat dissipation which leads to thermal gradients within the core cell of Li – ion batteries during their operation [49]. Recent studies have shown that thermal conduction within a battery core shell determines its overall heat dissipation [50]. It is believed that the thermal resistance between the cathode and separator interface is the limiting factor of the overall thermal conduction of

the battery cell. There is now a new focus in the material selection and design of the various components of a Li – ion battery. The current structure of a Li – ion battery cathode is a combination of electrochemically active electrode materials, carbon material, binder, and an aluminum foil or mesh used a current collector. This structure is known universally for achieving an effective electrochemical performance. However, current dry battery electrode materials have been shown to possess a low thermal conductivity value [51]. Previous studies showed that dry cathodes based on $Li[Ni_{1/3}Co_{1/3}Mn_{1/3}]O_2$ and multi walled carbon nanotubes (MWCNTs) possessed a cross plane thermal conductivity up to two orders of magnitude greater than conventional electrodes based on carbon black material [52]. Unfortunately, these Li – ion electrodes demonstrated a poor electrochemical performance. In the first part of this dissertation, we demonstrate that the incorporation of low dimensional (1D) carbon nanotubes in Li – ion cathodes based on $LiCoO_2$ show substantially improvement in the thermal properties of these cathodes without degrading their electrochemical performance.

1.2 Charge Density Wave Effects

The electron density of a metal is known to be highly uniform. As seen in Figure 1.1 a), the equilibrium positions of the atoms form a periodic lattice. Rudolf Peierls discovered that variations of the electron density in bulk metals require a significant amount of coulomb energy and are therefore suppressed [53]. In quasi – one and two – dimensional materials, local regions of high and low electron densities are known to be stable under

certain conditions. In some materials, the electron density spontaneously develops a modulation when the temperature drops below a specific transition temperature, T_c, as shown in Figure 1.1 b). This periodic modulation of the electronic charge density which is always accompanied by a periodic distortion of the atomic lattice in quasi – 1D and 2D metallic crystals is known as a macroscopic quantum state called a charge density wave (CDW). This symmetry reducing ground state is most commonly found in layered materials such as Tantalum disulfide (TaS_2). As previously examined, the crystal lattice of CDW materials undergo a periodic distortion which causes electrons to drop into a ground state where a periodic modulation of electronic charge density occurs. This modulation of charge results in the formation of an electronic energy gap at the fermi surface [54, 55].

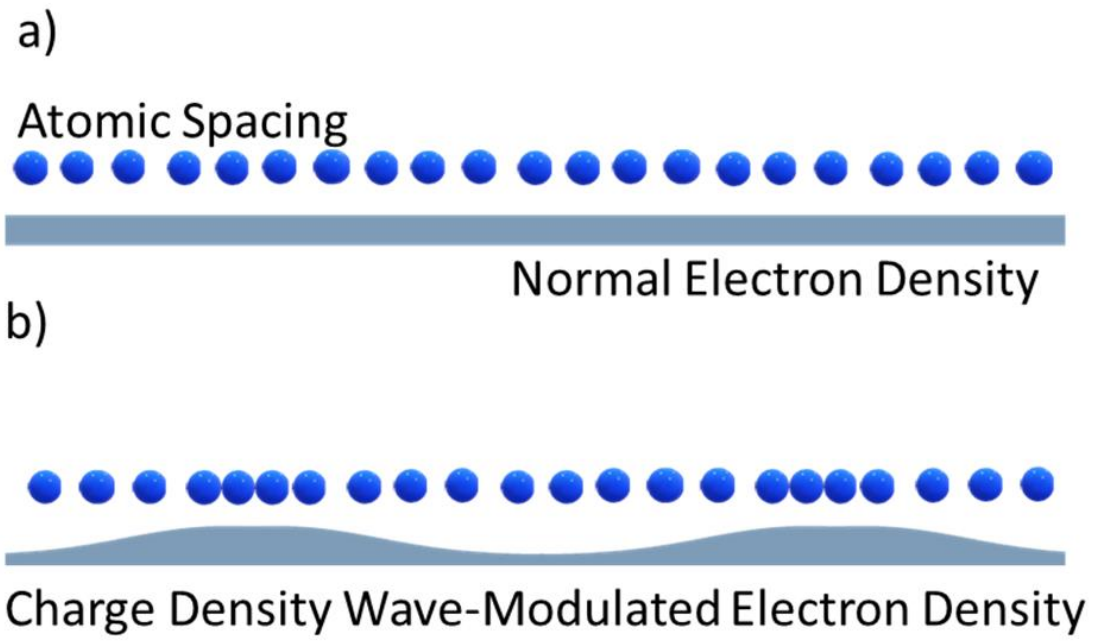

Figure 1.1: (a) Schematic of the normal state to the charge density wave state below the Peierls temperature, (b) and above the Peierls temperature.

At small applied electric fields, the CDW is pinned to defects on the underlying crystal lattice. However, at an applied field higher than that of a known threshold field, E_T, the CDW will de – pin from the defects of the underlying lattice and slide through the crystal, yielding a collective electrical current [56]. This intriguing property could have major implications as researchers start to search for new materials to reinvigorate the current semiconductor industry. As silicon based complementary metal – oxide – semiconductor (CMOS) technology scales down in size, energy dissipation has become a limiting factor. One switching cycle of a logic bit is represented by $NK_bT \; x \; ln(2)$ where N is the number of electrons, T is temperature and K_b is Boltzmann's constant [57, 58]. The governing physics of this limit implies that in silicon – based CMOS devices, electrons behave as independent charge carries and the energy dissipation limit would be reduced if electrons acted as a collective state. Consequently, CDW materials possess collective states that can be used to circumvent the power dissipation issues plaguing silicon – based CMOS transistors. In the second part of this dissertation, we report our findings on the investigation of current – voltage characteristics and low – frequency current fluctuations in vertical quasi – 2D $1T$ – TaS_2 CDW devices to increase the overall understanding of the governing physics of CDW phase transitions.

1.3 Overview

The introduction highlights the importance in investigating the thermal and electrical transport of low – dimensional advanced engineered materials and device structures to

solve pressing engineering problems. This dissertation is divided in two parts. In part 1, the thermal transport of Li – ion cathodes based on layered $LiCoO_2$ and MWCNTs material systems is explored. In part 2 of this dissertation, the electronic and noise characteristics of low – dimensional van der Waals materials will be studied to analyze their electronic performance as two terminal switching devices. Several device fabrication and characterization tools were used in this study.

1.4 References

[1] Richard Adolf Zsigmondy, *Colloids and the Ultramicroscope: A Manual of Colloid Chemistry and Ultramicroscop*, 1st ed. New York: J. Wiley & Sons, 1914.

[2] Bolotin, K. I., Sikes, K. J., Jiang, Z., Klima, M., Fudenberg, G., Hone, J., Kim, P., and Stormer, H. L., "Ultrahigh Electron Mobility in Suspended Graphene," *Solid State Commun.*, vol. 146, pp. 351–355, 2008.

[3] Geremew, A., Bloodgood, M. A., Aytan, E., Woo, B. W. K., Corber, S. R., Liu, G., Bozhilov, K., Salguero, T. T., Rumyantsev, S., Rao, M. P., and Balandin, A. A., "Current Carrying Capacity of Quasi – 1D $ZrTe_3$ van der Waals Nanoribbons," *IEEE Electron Device Lett.*, vol. 39, pp. 735–738, 2018.

[4] Liu, G., Debnath, B., Pope, T. R., Salguero, T. T., Lake, R. K., and Balandin, A. A., "A Charge – Density – Wave Oscillator Based on an Integrated Tantalum Disulfide–Boron Nitride – Graphene Device Operating at Room Temperature," *Nat. Nanotechnol.*, vol. 11, pp. 845–850, 2016.

[5] Liu, G., Zhang, E. X., Liang, C. D., Bloodgood, M. A., Salguero, T. T., Fleetwood, D. M., and Balandin, A. A., "Total – Ionizing – Dose Effects on Threshold Switching in 1*T* – TaS_2 Charge Density Wave Devices," *IEEE Electron Device Lett.*, vol. 38, pp. 1724–1727, 2017.

[6] Kargar, F., Barani, Z., Balinskiy, M., Magana, A. S., Lewis, J. S., and Balandin, A. A., "Dual – Functional Graphene Composites for Electromagnetic Shielding and Thermal Management," *Adv. Electron. Mater.*, vol. 5, p. 1800558, 2019.

[7] Balandin, A. A., Ghosh, S., Bao, W., Calizo, I., Teweldebrhan, D., Miao, F., and Lau, C. N., "Superior Thermal Conductivity of Single – Layer Graphene," *Nano Lett.*, vol. 8, pp. 902–907, 2008.

[8] Kim, K. S., Zhao, Y., Jang, H., Lee, S. Y., Kim, J. M., Kim, K. S., Ahn, J.–H., Kim, P., Choi, J.–Y., and Hong, B. H., "Large – Scale Pattern Growth of Graphene Films for Stretchable Transparent Electrodes," *Nature*, vol. 457, 706, 2009.

[9] Hochbaum, A. I. and Yang, P., "Semiconductor Nanowires for Energy Conversion," *Chem. Rev.*, vol. 110, pp. 527–546, 2010.

[10] Lin, Y.–M., Dimitrakopoulos, C., Jenkins, K. A., Farmer, D. B., Chiu, H.–Y., Grill, A., and Avouris, P., "100–GHz Transistors from Wafer–Scale Epitaxial Graphene," *Science*, vol. 327, 662, 2010.

[11] Liu, M., Yin, X., Ulin–Avila, E., Geng, B., Zentgraf, T., Ju, L., Wang, F., and Zhang, X., "A Graphene–Based Broadband Optical Modulator," *Nature*, vol. 474, 64, 2011.

[12] Geim, A. K. and Novoselov, K. S., "The Rise of Graphene," *Nat. Mater.*, vol. 6, 183, 2007.

[13] Garaj, S., Hubbard, W., Reina, A., Kong, J., Branton, D., and Golovchenko, J. A., "Graphene as a Subnanometre Trans–Electrode Membrane," *Nature*, vol. 467, 190, 2010.

[14] El–Kady, M. F., Strong, V., Dubin, S., and Kaner, R. B., "Laser Scribing of High–Performance and Flexible Graphene–Based Electrochemical Capacitors," *Science*, vol. 335, pp. 1326 – 1330, 2012.

[15] Yang, X., Xu, M., Qiu, W., Chen, X., Deng, M., Zhang, J., Iwai, H., Watanabe, E., and Chen, H., "Graphene Uniformly Decorated with Gold Nanodots: In Situ Synthesis, Enhanced Dispersibility and Applications," *J. Mater. Chem.*, vol. 21, pp. 8096–8103, 2011.

[16] Xu, M., Fujita, D., and Hanagata, N., "Perspectives and Challenges of Emerging Single–Molecule DNA Sequencing Technologies," *Small*, vol. 5, pp. 2638–2649, 2009.

[17] Xu, M., Gao, Y., Yang, X., and Chen, H., "Unique Synthesis of Graphene–Based Materials for Clean Energy and Biological Sensing Applications," *Chinese Sci. Bull.*, vol. 57, pp. 3000–3009, 2012.

[18] U.S. Energy Information Institution, "Annual Energy Outlook 2018 with Projections to 2050," 2018.

[19] Thackeray, M. M., Wolverton, C., and Isaacs, E. D., "Electrical Energy Storage for Transportation—Approaching the Limits of, and Going beyond, Lithium–Ion Batteries," *Energy Environ. Sci.*, vol. 5, pp. 7854–7863, 2012.

[20] Nair, N.–K. C. and Garimella, N., "Battery Energy Storage Systems: Assessment for Small–Scale Renewable Energy Integration," *Energy Build.*, vol. 42, pp. 2124–2130, 2010.

[21] Armand, M. and Tarascon, J.–M., "Building Better Batteries," *Nature*, vol. 451, 652, 2008.

[22] Lu, L., Han, X., Li, J., Hua, J., and Ouyang, M., "A Review on the Key Issues for Lithium–Ion Battery Management in Electric Vehicles," *J. Power Sources*, vol. 226, pp. 272–288, 2013.

[23] Hong, J., Maleki, H., Al Hallaj, S., Redey, L., and Selman, J. R., "Electrochemical-Calorimetric Studies of Lithium-Ion Cells," *J. Electrochem. Soc.* , vol. 145, pp. 1489–1501, 1998.

[24] Williford, R. E., Viswanathan, V. V, and Zhang, J.–G., "Effects of Entropy Changes in Anodes and Cathodes on the Thermal Behavior of Lithium Ion Batteries," *J. Power Sources*, vol. 189, pp. 101–107, 2009.

[25] Onda, K., Ohshima, T., Nakayama, M., Fukuda, K., and Araki, T., "Thermal Behavior of Small Lithium–Ion Battery during Rapid Charge and Discharge Cycles," *J. Power Sources*, vol. 158, pp. 535–542, 2006.

[26] Reynier, Y., Yazami, R., and Fultz, B., "The Entropy and Enthalpy of Lithium Intercalation into Graphite," *J. Power Sources,* vol. 119–121, pp. 850–855, 2003.

[27] Lu, W., Belharouak, I., Liu, J., and Amine, K., "Thermal Properties of $Li_{4/3}Ti_{5/3}O_4$/$LiMn_2O_4$ Cell," *J. Power Sources,* vol. 174, pp. 673–677, 2007.

[28] Yazami, R., Reynier, Y., and Fultz, B., "Entropymetry of Lithium Intercalation in Spinel Manganese Oxide: Effect of Lithium Stoichiometry," *ECS Trans.*, vol. 1, pp. 87–96, 2006.

[29] Funahashi, A., Kida, Y., Yanagida, K., Nohma, T., and Yonezu, I., "Thermal Simulation of Large–Scale Lithium Secondary Batteries Using a Graphite–Coke Hybrid Carbon Negative Electrode and $LiNi_{0.7}Co_{0.3}O_2$ Positive Electrode," *J. Power Sources,* vol. 104, pp. 248–252, 2002.

[30] Reynier, Y., Graetz, J., Swan–Wood, T., Rez, P., Yazami, R., and Fultz, B., "Entropy of Li Intercalation in Li_xCoO_2," *Phys. Rev. B,* vol. 70, 174304, 2004.

[31] Viswanathan, V. V, Choi, D., Wang, D., Xu, W., Towne, S., Williford, R. E., Zhang, J.–G., Liu, J., and Yang, Z., "Effect of Entropy Change of Lithium Intercalation in Cathodes and Anodes on Li–Ion Battery Thermal Management," *J. Power Sources,* vol. 195, pp. 3720–3729, 2010.

[32] Burheim, O. S., Onsrud, M. A., Pharoah, J. G., Vullum–Bruer, F., and Vie, P. J. S., "Thermal Conductivity, Heat Sources and Temperature Profiles of Li–Ion Batteries," *ECS Trans.*, vol. 58, pp. 145–171, 2014.

[33] Feng, X., Ouyang, M., Liu, X., Lu, L., Xia, Y., and He, X., "Thermal Runaway Mechanism of Lithium Ion Battery for Electric Vehicles: A Review," *Energy Storage Mater.*, vol. 10, pp. 246–267, 2018.

[34] Wang, Q., Ping, P., Zhao, X., Chu, G., Sun, J., and Chen, C., "Thermal Runaway Caused Fire and Explosion of Lithium Ion Battery," *J. Power Sources,* vol. 208, pp. 210–224, 2012.

[35] Xu, X. M., Li, R. Z., Zhao, L., Hu, D. H., and Wang, J., “Probing the Thermal Runaway Triggering Process within a Lithium–Ion Battery Cell with Local Heating,” *AIP Adv.*, vol. 8, 105323, 2018.

[36] Williard, N., He, W., Hendricks, C., and Pecht, M., “Lessons Learned from the 787 Dreamliner Issue on Lithium–Ion Battery Reliability,” *Energies* , vol. 6, pp. 4682–4695, 2013.

[37] Mahamud, R. and Park, C., “Reciprocating Air Flow for Li–Ion Battery Thermal Management to Improve Temperature Uniformity,” *J. Power Sources*, vol. 196, pp. 5685–5696, 2011.

[38] Chen, Y. and Evans, J. W., “Heat Transfer Phenomena in Lithium/Polymer-Electrolyte Batteries for Electric Vehicle Application,” *J. Electrochem. Soc.*, vol. 140, pp. 1833 Chen, Y. and Evans, J. W., “Heat Transfer Phenomena in Lithium/Polymer-Electrolyte Batteries for Electric Vehicle Application,” *J. Electrochem. Soc.*, vol. 140, pp. 1833–1838, 1993.

[39] Zolot, M., Pesaran, A. A., and Mihalic, M., “Thermal Evaluation of Toyota Prius Battery Pack.” SAE International, pp. 923–928, 2002.

[40] Kelly, K.J., Mihalic, M. and Zolot, M., "Battery usage and thermal performance of the Toyota Prius and Honda Insight during chassis dynamometer testing," *Seventeenth Annual Battery Conference on Applications and Advances. Proceedings of Conference (Cat. No.02TH8576)*, Long Beach, CA, USA, 2002, pp. 247–252.

[41] Zolot, M., Kelly, K., Keyser, M., Mihalic, M., Zolot, K., Keyser, M., Mihalic, M., and Pesaran, A., “Thermal Evaluation of the Honda Insight Battery Pack,” in *36th Intersociety Energy Conversion Engineering Conference*, pp. 1833–1838, 2001.

[42] Pesaran, A. A., Burch, S. D., and Keyser, M., “An Approach for Designing Thermal Management Systems for Electric and Hybrid Vehicle Battery Packs,” *Fourth Veh. Therm. Manag. Syst. Conf. Exhib.*, pp. 1–18, 1999.

[43] Tran, T.–H., Harmand, S., Desmet, B., and Filangi, S., "Experimental Investigation on the Feasibility of Heat Pipe Cooling for HEV/EV Lithium–Ion Battery," *Appl. Therm. Eng.*, vol. 63, pp. 551–558, 2014.

[44] Barantsevich, V. and Shabalkin, V., "Heat Pipes for Thermal Control of ISS Solar Battery Drive," *Appl. Therm. Eng.*, vol. 23, pp. 1119–1123, 2003.

[45] Wu, M.–S., Liu, K. H., Wang, Y.–Y., and Wan, C.–C., "Heat Dissipation Design for Lithium–Ion Batteries," *J. Power Sources*, vol. 109, pp. 160–166, 2002.

[46] Sabbah, R., Kizilel, R., Selman, J. R., and Al–Hallaj, S., "Active (Air–Cooled) vs. Passive (Phase Change Material) Thermal Management of High Power Lithium–Ion Packs: Limitation of Temperature Rise and Uniformity of Temperature Distribution," *J. Power Sources*, vol. 182, pp. 630–638, 2008.

[47] Khateeb, S. A., Amiruddin, S., Farid, M., Selman, J. R., and Al–Hallaj, S., "Thermal Management of Li–Ion Battery with Phase Change Material for Electric Scooters: Experimental Validation," *J. Power Sources*, vol. 142, pp. 345–353, 2005.

[48] Hallaj, S. Al and Selman, J. R., "A Novel Thermal Management System for Electric Vehicle Batteries Using Phase-Change Material," *J. Electrochem. Soc.* , vol. 147, pp. 3231–3236, 2000.

[49] Ramadass, P., Haran, B., Gomadam, P. M., White, R., and Popov, B. N., "Development of First Principles Capacity Fade Model for Li–Ion Cells," *J. Electrochem. Soc.*, vol. 151, pp. A196–A203, 2004.

[50] Vishwakarma, V., Waghela, C., Wei, Z., Prasher, R., Nagpure, S. C., Li, J., Liu, F., Daniel, C., and Jain, A., "Heat Transfer Enhancement in a Lithium–Ion Cell through Improved Material–Level Thermal Transport," *J. Power Sources*, vol. 300, pp. 123–131, 2015.

[51] Garimella, S. V, Fleischer, A. S., Murthy, J. Y., Keshavarzi, A., Prasher, R., Patel, C., Bhavnani, S. H., Venkatasubramanian, R., Mahajan, R., Joshi, Y., Sammakia, B., Myers, B. A., Chorosinski, L., Baelmans, M., Sathyamurthy, P., and Raad, P. E., "Thermal Challenges in Next–Generation Electronic Systems," *IEEE Trans. Components Packag. Technol.*, vol. 31, pp. 801–815, 2008.

[52] Koo, B., Goli, P., Sumant, A. V, dos Santos Claro, P. C., Rajh, T., Johnson, C. S., Balandin, A. A., and Shevchenko, E. V, "Toward Lithium Ion Batteries with Enhanced Thermal Conductivity," *ACS Nano*, vol. 8, pp. 7202–7207, 2014.

[53] Peierls, R. E. and Roberts, L. D., "*Quantum Theory of Solids*," *Phys. Today*, vol. 9, pp. 29–29, 1956.

[54] Wilson, J. A., Di Salvo, F. J., and Mahajan, S., "Charge–Density Waves in Metallic, Layered, Transition–Metal Dichalcogenides," *Phys. Rev. Lett.*, vol. 32, pp. 882–885, 1974.

[55] Grüner, G., "The Dynamics of Charge–Density Waves," *Rev. Mod. Phys.*, vol. 60, pp. 1129–1181, 1988.

[56] Goli, P., Khan, J., Wickramaratne, D., Lake, R. K., and Balandin, A. A., "Charge Density Waves in Exfoliated Films of van der Waals Materials: Evolution of Raman Spectrum in $TiSe_2$," *Nano Lett.*, vol. 12, pp. 5941–5945, 2012.

[57] Salahuddin, S. and Datta, S., "Interacting Systems for Self–Correcting Low Power Switching," *Appl. Phys. Lett.*, vol. 90, 93503, 2007.

[58] Zhirnov, V. V, Cavin, R. K., Hutchby, J. A., and Bourianoff, G. I., "Limits to Binary Logic Switch Scaling – a Gedanken Model," *Proc. IEEE*, vol. 91, pp. 1934–1939, 2003.

Chapter 2

2 Thermal Characterization Methodology

2.1 Introduction to Thermal Conductivity

Heat is an incoherent form of energy that relates to the internal energy of matter which moves from one region to another by three methods. Internal energy can be transferred by diffusion, convection and radiation [1]. The diffusion of energy is commonly known as heat conduction and is defined as the transfer of internal energy from a hot to cold region. In fluids, the internal energy of a matter is transferred by convection. Lastly, internal energy can be transferred as electromagnetic radiation. This work will focus mainly on heat conduction. In engineering, the ability to conduct heat is as a material property known as thermal conductivity. It is defined based on the terms of Fourier's law of heat conduction in which a heat flux ($\vec{q}$) is equal to the negative product of a local temperature gradient (ΔT) and thermal conductivity (K) [2]:

$$\vec{q} = -K\Delta\mathrm{T} \tag{2.1}$$

The units of thermal conductivity are in watt per kelvin per meter ($\mathrm{Wm^{-1}K^{-1}}$). Another important material property which defines heat transport in a solid is thermal diffusivity

(λ). The thermal diffusivity of an object is defined as its thermal conductivity divided by its specific heat capacity C_p, and density (ρ) [2]:

$$\lambda = \frac{K}{\rho C_p} \tag{2.2}$$

The units for thermal diffusivity are in meter squared per second (m^2s^{-1}). In short, thermal diffusivity is a property which describes how fast heat will flow in a material, while thermal conductivity defines the quantity of heat flow.

Heat is conducted through a solid material by either free charge carriers (electrons) or by elastic waves characterized by crystal lattice vibrations (phonons). In a semiconductor material, the thermal conductivity (K) has both components contributed by electron (K_e) and photons (K_p) [1]:

$$K = K_e + K_p \tag{2.3}$$

In metals, heat is carried mostly by free electrons, while in semiconductors heat conductance is mostly contributed by phonons. In some materials, phonons and electrons can have comparable contribution to the total thermal conductivity [3]. The thermal conductivity of materials varies widely from as high as ~ 3000 $Wm^{-1}K^{-1}$ for graphene to as low as ~ 0.01 $Wm^{-1}K^{-1}$ for aerogels [4]. The thermal conductivity of materials is also directional (anisotropic) and temperature dependent.

2.2 Methods of Measuring Thermal Conductivity

Since the mid–20th century, there have been many extensive studies on the thermal characterization of bulk materials [5–8]. Consequently, there are many methods used to measure the thermal conductivity of a material. The most widely known methods can be divided into two categories; steady state and transient methods. In the steady state method, the thermal properties of a material are measured by creating a temperature gradient that is independent of time. Transient methods normally measure the time dependent heat dissipation to characterize its material properties. The steady state methods have glaring issues such as high parasitic heat losses, high sensor contact resistance, and very long wait times to establish steady state temperature conditions. For this reason, this work discusses transient method – based thermal characterization. The following sections focuses on the two most commonly used transient methods known as the transient plane source (TPS) technique, which measures the average in–plane thermal conductivity and the laser flash thermal diffusivity method, which measures the average cross plane thermal conductivity.

2.3 Transient Plane Source Technique

The transient plane source technique, also known as Hot Disk, is a transient technique used to measure the thermal properties of materials [9,10]. It follows the International Organization for Standardization (ISO) method 22007–2:2015. The Hot Disk is a non –

destructive method to measure the average in – plane thermal conductivity and thermal diffusivity of a solid, liquid or powder material. These thermal properties vary on the temperature and direction of the material. The Hot Disk can measure a wide range of thermal conductivities from 0.005 $Wm^{-1}K^{-1}$ to 1000 $Wm^{-1}K^{-1}$ over a wide temperature range. The main component in the Hot Disk system is the sensor which consist of a flat resistive nickel element with a double spiral geometry which is sandwiched between two layers of Kapton, as seen in Figure 2.1. The Kapton acts as both an electrical insulator and mechanical support. Nickel is chosen because of its widely reported temperature coefficient of resistivity (TCR). The nickel sensor behaves as both a heat source and a temperature monitor. The Hot Disk coil has a temperature coefficient which can be deduced by observing a resistance recording.

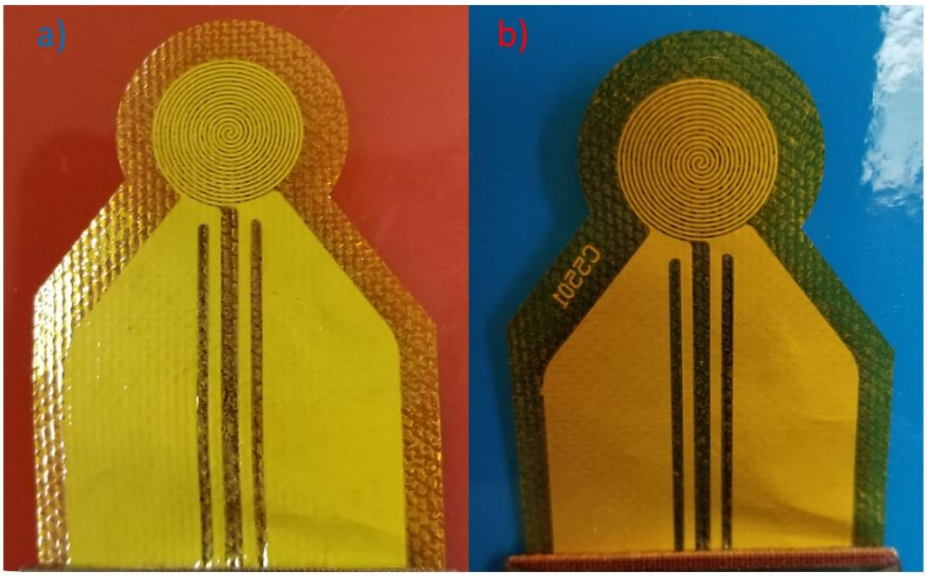

Figure 2.1: a) A photograph of a typical Hot Disk sensor consisting of a nickel spiral and four terminals, encapsulated by a Kapton film. b) A Hot Disk sensor with a larger diameter. Hot Disk sensors are available in a variety of spiral diameters, ranging from 0.5 mm to 29.5 mm.

The sensor is placed in between two identical pieces of a sample to begin the measurement and enough time is given to allow the sensor and the sample to reach thermal equilibrium. During the measurement, a pulse of current is transmitted through the nickel element which generates joule heating. The generated heat dissipates through the two pieces of the sample at a rate which depends on the thermal transport properties of the sample. The measured temperature increase in the sensor is monitored with high precision and accuracy by measuring its electrical resistivity. The sensor is usually heated from 0.5 K to 5 K, while the temperature dependent electrical resistivity is recorded. The average temperature rise on the surface of the sensor, $\overline{\Delta T(\tau)}$, is measured from the temperature—based electrical resistance of the nickel element, $R(t)$, and temperature coefficient of resistivity by the expression [11]:

$$R(t) = R_o[1 + \alpha\overline{\Delta T(\tau)}] \tag{2.4}$$

As seen in Figure 2.2, the heat generated from the sensor dissipates in all direction of the contacting sample surfaces. Theoretically, the Hot Disk sensor can be mathematically approximated as a sensor with n number of concentric rings which are equally spaced and provide a uniform power distribution. If a is the radius of the largest ring, the radius of the smallest ring is a divided by n. The total length of the nickel element, L, is then [11]:

$$L = \sum_{l=1}^{n} 2\pi l \frac{a}{n} = (n+1)\pi a \tag{2.5}$$

Using the equation of heat conduction and the well–known instantaneous point source solution, the temperature increase on the surface of the Hot Disk sensor is extracted by integrating the point source solution over time and the volume of the source. The average

temperature increase of the sensor can be calculated by averaging the temperature rise of a ring source over the length of the concentric rings [11]. The time dependent temperature increase of the sensor, $\overline{\Delta T(\tau)}$, is then expressed as:

$$\overline{\Delta T(\tau)} = \frac{P_o}{\pi^{\frac{3}{2}} aK} D(\tau) \tag{2.6}$$

Here P_o is the total power provided by the sensor, a is the radius of the sensor, K is the thermal conductivity of the measured sample, and $D(\tau)$ is a dimensionless time dependent function described by:

$$D(\tau) = [n(n+1)]^{-2} \int_0^r \sigma^{-2} d\sigma [\sum_{l=1}^{n} l \sum_{k=1}^{k} kexp\{\frac{-(l^2+k^2)}{4n^2\sigma^2}\} I_o \{\frac{lk}{2n^2\sigma^2}\} \tag{2.7}$$

The term τ is a characteristic time constant represented as:

$$\tau = \frac{\sqrt{\lambda t}}{a} \tag{2.8}$$

where λ is thermal diffusivity, and t is the total transient recording time.

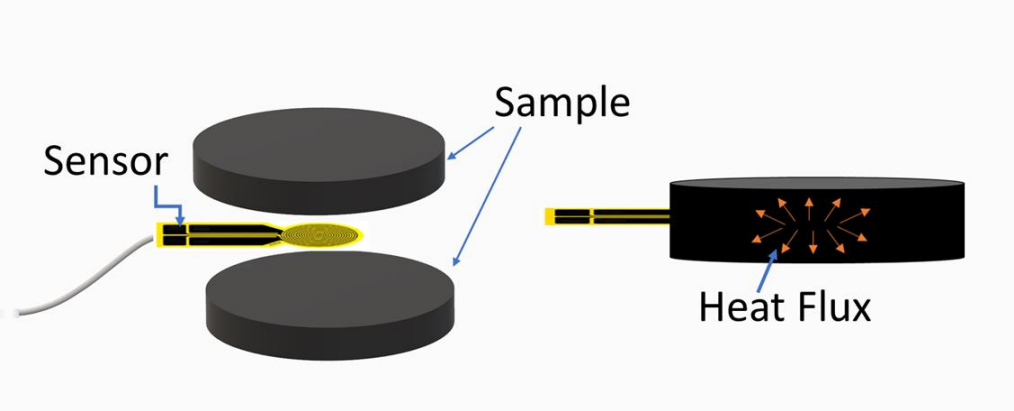

Figure 2.2: A schematic of a Hot Disk sensor in between two identical pieces of a sample. The diameter of the sensor is chosen in consideration of the samples geometry to avoid any influence by the boundary of the sample.

As shown by equation (2.6), the thermal conductivity of a sample measured using the transient plane source technique can be obtained from the linear plot of $\overline{\Delta T(\tau)}$ as a function of $D(\tau)$. Since the slope of this line is $\frac{P_o}{\pi^{\frac{3}{2}} aK}$, the input power, P_o, and radius of the sensor are known, the thermal conductivity, K, can be calculated. This is done by experimentally measuring the temperature increase of a range of input power values, P_o, and recording time, t, until a linear relationship with the maximum correlation coefficient between $\overline{\Delta T(\tau)}$ and $D(\tau)$ is observed, as this would yield the optimized value of thermal conductivity. Thermal diffusivity, λ, can then be calculated by equation (2.8) using the optimized transient recording time and known sensor radius. This process can be run iteratively by software and both the thermal conductivity and diffusivity can be obtained using the transient plane source technique. Knowing the density of the measured sample, the specific heat can be calculated using equation (2.2). The transient plane source technique has been successfully used to measure the thermal properties of various materials [12–15]. In this dissertation, it has been used to measure the average in–plane thermal conductivity of novel li – ion battery cathodes.

2.4 Laser Flash Technique

The laser flash technique is an optical transient method of measuring the average cross–plane thermal conductivity of a material. As seen in Figure 2.3, the laser flash technique consist of a xenon flash lamp which provides a uniform heat pulse, with a duration

compared to the transient time, through the rear side. The sample's temperature rise is up to 2K and is measured using a nitrogen cooled indium antimonide (InSb) infra – red detector, on the front face of the sample. If we assume no heat loses, the normalize temperature increase on the front face of the sample is given by:

$$T/T_{max} = 1 + 2\sum_{m=1}^{\infty}(-1)^m \exp(-m^2\omega) \qquad (2.9)$$

where $\omega = \pi^2\alpha t/L^2$, T is the instantaneous temperature increase in the front face of the sample, T_{max} is the maximum temperature increase of the front face of the sample, and L is the sample thickness. By knowing the thermal pulse propagation time, the thermal diffusivity, α, can be measured by the expression:

$$\alpha = 0.1388\frac{L^2}{t_{\frac{1}{2}}} \qquad (2.10)$$

where $t_{\frac{1}{2}}$ is the half–maximum time of the temperatures rise. Using equation (2.2) and the density and specific heat of an investigated sample, the thermal conductivity can be

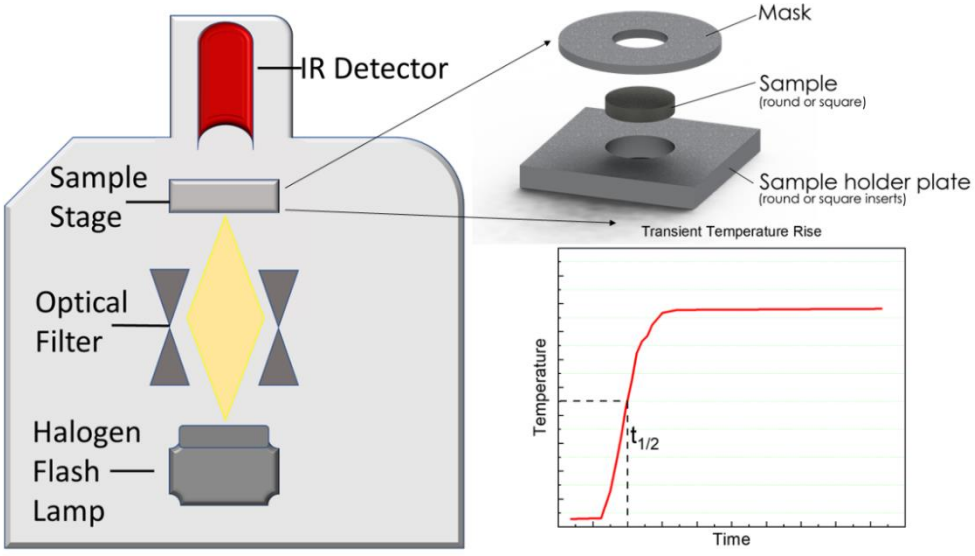

Figure 2.3: A schematic of a Laser Flash instrument showing the integral components which are used to measure the transient temperature rise of sample. An example of a transient temperature plot can be seen in the bottom right.

calculated. The laser flash instrument has been widely used to measure the thermal diffusivity of a variety of samples [16–18] and has been used to measure the average cross plane thermal conductivity of carbon nanotube based Li–ion cathode materials.

2.5 References

[1] Incropera, F. P., DeWitt, D. P., Bergman, T. L., and Lavine, A. S., "Fundamentals of Heat and Mass Transfer," John Wiley & Sons, Inc., 2007.

[2] Tritt, T.M., "Thermal Conductivity: Theory, Properties, and Applications," Kluwer Academic/Plenum Publishers, 2004

[3] Goldsmid, H. J., "The Thermal Conductivity of Bismuth Telluride," *Proc. Phys. Soc. Sect. B*, vol. 69, pp. 203–209, 1956.

[4] Cuce, E., Cuce, P. M., Wood, C. J., and Riffat, S. B., "Toward Aerogel Based Thermal Superinsulation in Buildings: A Comprehensive Review," *Renewable and Sustainable Energy Reviews*., vol. 34, pp. 273–299, 2014.

[5] Zeller, R. C. and Pohl, R. O., "Thermal Conductivity and Specific Heat of Noncrystalline Solids," *Phys. Rev. B*, vol. 4, pp. 2029–2041, 1971.

[6] Madhusudana, C.V., and Fletcher, L.S., "Contact Heat Transfer – The Last Decade," *AIAA J.*, vol. 24, pp. 510–523, 2008.

[7] Hamilton, R. L., "Thermal Conductivity of Heterogeneous Two–Component Systems," *Ind. Eng. Chem. Fundam.*, vol. 1, pp. 187–191, 1962.

[8] Cooper, M. G., Mikic, B. B., and Yovanovich, M. M., "Thermal Contact Conductance," *Int. J. Heat Mass Transf.*, vol. 12, pp. 279–300, 1969.

[9] Gustavsson, M., Karawacki, E., and Gustafsson, S. E., "Thermal Conductivity, Thermal Diffusivity, and Specific Heat of Thin Samples from Transient Measurements with Hot Disk Sensors," *Rev. Sci. Instrum.*, vol. 65, pp. 3856–3859, 1994.

[10] Gustafsson, S. E., "Transient Plane Source Techniques for Thermal Conductivity and Thermal Diffusivity Measurements of Solid Materials," *Rev. Sci. Instrum.*, vol. 62, pp. 797–804, 1991.

[11] H. S. Carslaw, J. C. J., "Conduction of Heat in Solids," *Oxford Clarendon Press.*, 1959.

[12] Goyal, V. and Balandin, A. A., "Thermal Properties of the Hybrid Graphene–Metal Nano–Micro–Composites: Applications in Thermal Interface Materials," *Appl. Phys. Lett.*, vol. 100, 73113, 2012.

[13] Ramirez, S., Chan, K., Hernandez, R., Recinos, E., Hernandez, E., Salgado, R., Khitun, A. G., Garay, J. E., and Balandin, A. A., "Thermal and Magnetic Properties of Nanostructured Densified Ferrimagnetic Composites with Graphene – Graphite Fillers," *Mater. Des.*, vol. 118, pp. 75–80, 2017.

[14] Goyal, V., Subrina, S., Nika, D.L., and Balandin, A.A., "Reduced Thermal Resistance of the Silicon–synthetic Diamond Composite Substrates at Elevated Temperatures," Appl. Phys. Lett. vol. 97, 031904, 2010.

[15] Ghosh, S., Teweldebrhan, D., Morales, J. R., Garay, J. E., and Balandin, A. A., "Thermal Properties of the Optically Transparent Pore–Free Nanostructured Yttria–Stabilized Zirconia," *J. Appl. Phys.*, vol. 106, 113507, 2009.

[16] Renteria, J. D., Ramirez, S., Malekpour, H., Alonso, B., Centeno, A., Zurutuza, A., Cocemasov, A. I., Nika, D. L., and Balandin, A. A., "Strongly Anisotropic Thermal Conductivity of Free–Standing Reduced Graphene Oxide Films Annealed at High Temperature," *Adv. Funct. Mater.*, vol. 25, pp. 4664–4672, 2015.

[17] Renteria, D. J., Nika, L. D., and Balandin, A. A., "Graphene Thermal Properties: Applications in Thermal Management and Energy Storage," *Applied Sciences* , vol. 4, pp. 525–547, 2014.

[18] Goli, P., Ning, H., Li, X., Lu, C. Y., Novoselov, K. S., and Balandin, A. A., "Thermal Properties of Graphene–Copper–Graphene Heterogeneous Films," *Nano Lett.*, vol. 14, pp. 1497–1503, 2014.

Chapter 3

3 Carbon Nanotube Lithium Ion Cathodes

3.1 Introduction

The first Li–ion battery was created in 1976 [1]. In 1991, Nitta *et al* [2] demonstrated the first commercial rechargeable Li–ion battery. A number of recent advancements have led to the overall improvement in high power density Li–ion batteries [3–6]. Since then, rechargeable Li–ion batteries have become immensely popular and are in heavy use in aircrafts and electric vehicles. Although Li–ion batteries are highly efficient in converting chemical stored energy into electric potential, there is still a significant amount of energy loss due to ohmic heating as electric current is transmitted through the internal resistance of the cell [7–9]. In addition to joule heating, heat can be generated from the chemical reactions taking place within the battery cell during charging and discharging; cathodes are particularly susceptible to this type of heating [10–12]. To avoid the risk of overheating, Li–ion batteries are normally coupled with thermal management systems which can complicate the overall design at the pack level. Additionally, these systems do little to improve heat dissipation at the materials level and do not improve the safety of individual cells. It was previously shown that the low heat conduction across the interface of the

cathode and mating surfaces limit the heat dissipation of the overall cell [13]. Therefore, the focus of the chapter is to improve the overall heat conduction within a cell by fabricating and testing Li–ion cathodes with exceptional thermal conductivity.

The conventional design of Li–ion cathodes are based on the laminate composite film structure and consists of an electrochemically active material, conductive carbon material and a polymer binder, all of which are coated on an aluminum of copper foil current collector [14]. The carbon content in this design takes up a large volume fraction, as its role is to ensure a good electrical contact between the active materials and the metal current collector. The carbon material of choice in conventional Li–ion cathode structures is carbon black. Carbon black is a very poor thermal conductor, as it possesses a thermal conductivity value between 0.1 to 1 $Wm^{-1}K^{-1}$ at room temperature, which lowers the overall thermal dissipation property of the entire cathode assembly [15]. The overall thermal conductivity of current cathode electrodes ranges from 0.3 to 0.8 $Wm^{-1}K^{-1}$ [16–17]. To address this concern, a suitable alternative to carbon black such as other more thermally conductivity carbon allotropes should be studied. In the upper echelon of highly, thermally conductive carbon allotropes lies graphene and carbon nanotubes [18]. Single layer graphene, observed as a single atomic sheet of graphite, has a reported thermal conductivity value ranging from 2000 to 5000 $Wm^{-1}K^{-1}$ [19], However, using single layer graphene in a cathode laminate structure may lead to problems due to Li–ion cell electrolyte diffusion [20]. Alternatively, carbon nanotubes which have a reported thermal conductivity from 1,750 to 5,800 $Wm^{-1}K^{-1}$ [21], have shown a greater electrical conductivity enhancement in compacted structures than graphene layers.

In this section we show that composite cathodes fabricated from commercial 100 mm long carbon nanotubes (CNTs) and $LiCoO_2$ (LCO) particles reveal an in – plane thermal conductivity around ~200 $Wm^{-1}K^{-1}$. This value exceeds the thermal conductivity of conventional dry laminated cathodes by roughly three orders of magnitude. The cross–plane thermal conductivity of CNT–based cathodes is approximately the same as that of conventional dry laminate cathodes. The CNT–based cathodes reveal a similar electrochemical capacity as conventional laminated cathodes but possess a superior rate performance and cycling stability. The addition of micro and nano sized diamond particles in CNT–based cathodes improves the rate performance. The lightweight, flexible design of our fabricated CNT–based cathodes provide a new platform for assembling Li–ion electrodes from a range of electrochemically active materials with superior heat dissipating properties and that are binder – less and free of any aluminum or copper current collectors.

3.2 Carbon Nanotube Lithium Ion Cathode Fabrication

Unmodified $LiCoO_2$ (LCO) particles were purchased from Sigma–Aldrich. C–grade long multi–walled CNTs (100 μm in length and 5 to 30 nm in diameter) and short multi walled CNTs (5 μm in length and 6 to 9 nm in diameter) were purchased from NanotechLab. Nano size diamonds (~2 nm) and micron size (8 to 16 μm) diamond particles were purchased from International Technology Center and Raleigh & NC Diamond Innovations, respectively. A corresponding amount of each material was dispersed in a 250ml isopropyl alcohol (IPA) solution and sonicated for 20 min. The solution was then vacuum filtrated

on a microporous glass fiber filter (Wachman GF–F). The filtrated suspension results in a black CNT film deposited on the glass fiber filter. The samples were then annealed in air for 12 hours, resulting in the several layered structures schematically illustrated in Figure 3.1. After fabricating several carbon nanotube – based cathodes, four different cathode samples, which were observed to be the most robust performers during electrochemical tests, were selected for further in – depth thermal conductivity and electrochemical testing. Among these four structures, a control sample (CNT) was fabricated using 10 mg of CNTs. To investigate the interaction between CNTs and $LiCoO_2$, a cathode structure (CNTLCO) consisting of 51 mg of $LiCoO_2$ particles mixed together with 2 mg of CNTs and then sandwiched between two layers consisting of 4 mg of CNTs was fabricated. Samples CNTLCOND and CNTLCOMD, consisting of nano and micro sized diamond particles, were fabricated to improve the cross – sectional thermal conductivity. All cathodes were fabricated without a binder while the CNT matrix acted as a current collector. This description follows the work described in [22].

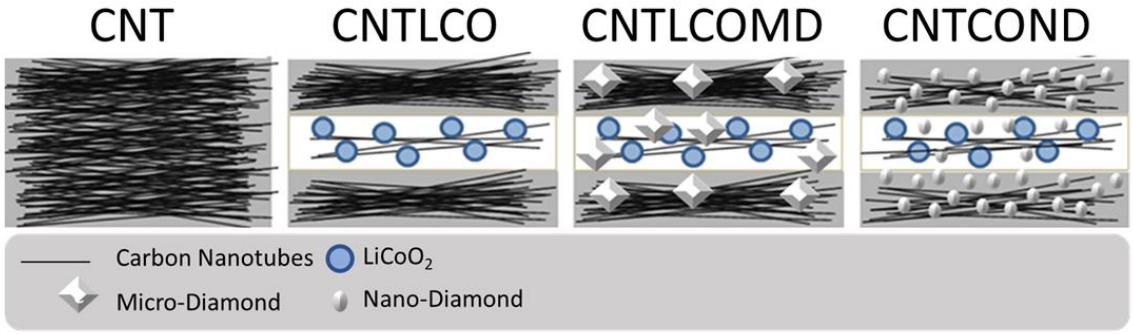

Figure 3.1: Schematic depicting the various layered structures which were fabricated for electrochemical and thermal conductivity testing. The electrochemical and thermal conduction contributions of long carbon nanotubes, micro and nano size diamonds were investigated against various control samples, consisting of cathodes structures of pure carbon nanotubes.

3.3 Thermal Analysis of Carbon Nanotube Cathodes

The thermal conductivity of the fabricated cathode samples was experimentally measured using two different transient techniques: The Hot Disk based on the transient plane source technique, and the Laser Flash analysis. Due to the complicated layered structure of the samples and the physical limitations of the Hot Disk instrument, the in – plane and cross – plane thermal conductivity could only be measured at room temperature. Figure 3.2 shows photographs of the sample along with the components of the Hot Disk instrument.

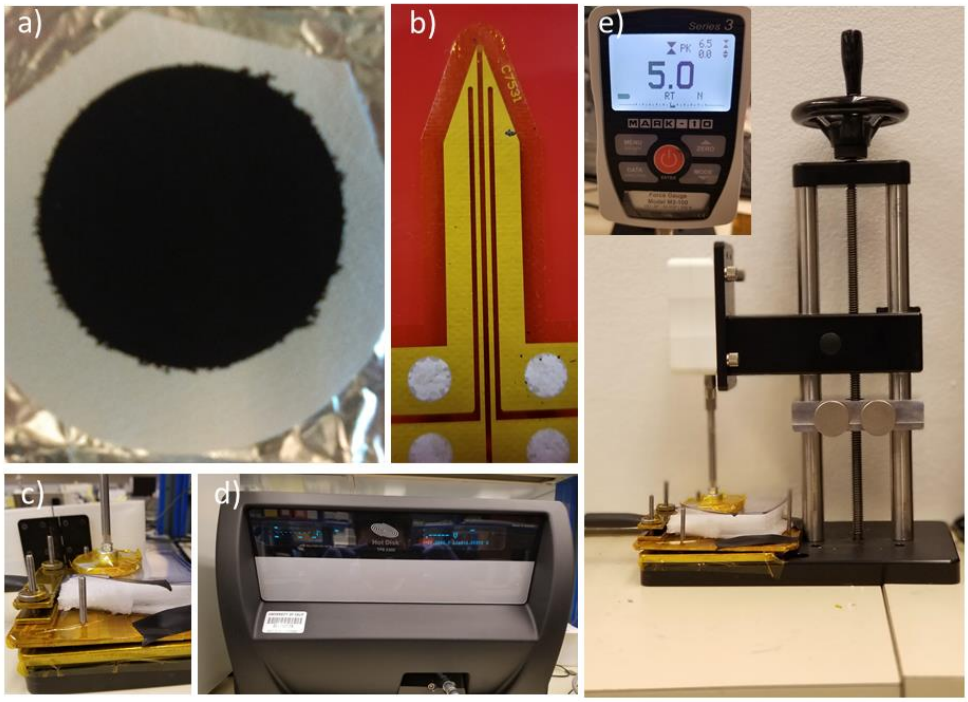

Figure 3.2: A photograph of a) a typical black CNT based cathode on a white fiber glass filter, b) a typical Hot Disk sensor, c) the Hot Disk sample holder which houses the sensor pressed in between two pieces of the cathode material, insulated with stereofoam and kapton material, d) the Hot Disk module, and e) the mechanical press and pressure gauge used to ensure a good thermal contact between the sensor and the sample surfaces.

For the in – plane thermal conductivity measurements, samples were prepared folding the stand – alone cathodes in between the Hot Disk sensor. The sample was then placed on an insulated test platform and encapsulated with insulating material to avoid temperature drift effects from the surrounding environment. A mechanical press and a Mark–10 force gauge was used to ensure uniform and stable pressure between the sample and the Hot Disk sensor, ensuring good surface and thermal contact. A significant time was allowed in between tests to ensure the sensor and the sample surfaces reach equilibrium temperature. The thermal diffusivity and thermal conductivity of the electrodes were calculated by recording the temperature rise as a function of time using equation (2.6). The power dissipated by the sensor and recording time were chosen from an iterative process so that the heat flux within the cathodes and the temperature rise of the sensor are not influenced by the boundaries of the cathode. Each cathode was measured several times to ensure reproducibility of measured results.

The carbon nanotube–based cathodes' cross–plane thermal conductivity was measured using an optical Laser Flash technique (LF, Netzsch). To measure its thermal diffusivity, an electrode sample is placed into a stage and a xenon flash lamp produces shots of energy of 10 joules/pulse on the electrode surface while it's temperature rise is monitored at the opposite end with a liquid nitrogen cooled In – Sb (Indium – Antimonide) infra – red detector. The temperature evolution on the rear of the electrode is recorded and converted into an amplified signal. A mathematical model (Cowan model) was used to fit the recorded curve to determine the thermal diffusivity and the thermal conductivity was

calculated from the equation $K=\rho\alpha C_p$, where ρ is the electrode's mass density, and C_p is its specific heat (measured separately).

Before the thermal properties of CNT – based samples were measured, the thermal conductivity of well – defined standards were measured using Hot Disk and Laser Flash for calibration. As seen in Table 1, the thermal conductivities measured for standard materials at room temperature are close agreement with their reported values. It is important to note that that Hot Disk and Laser Flash require different materials as standards. Figure 3.3 reveals the in – plane and cross – plane thermal conductivity values for CNT–based $LiCoO_2$ and a control CNT sample. The CNTLCO electrode sample is shown to have an in – plane thermal conductivity value as high as ~200 $Wm^{-1}K^{-1}$ (comparable to aluminum). Aluminum is a known material used as a current collector in Li–ion cells and an effective heat sink. The thermal conductivity value measured on our fabricated electrodes is around three orders higher than traditional laminate electrodes.

Table 3.1: Thermal conductivity values of reference samples. Reprinted with permission from E. Lee, R.A. Salgado, B. Lee, A. V. Sumant, T. Rajh, C. Johnson, A.A. Balandin, E. V. Shevchenko, "Design of lithium cobalt oxide electrodes with high thermal conductivity and electrochemical performance using carbon nanotubes and diamond particles," Carbon, Vol. 129, pp. 702-710. 2018. Copyright © 2018 Elsevier.

Test	Material	kW/m*K	±
LFA	Pyroceram	4.01	0.04
LFA	Pyrex	1.01	0.03
LFA	Poco-graphite AXM-5Q	91.7	0.02
Hot disk	Stainless Steel	13.48	0.03
Hot disk	Silicon	143.86	0.03

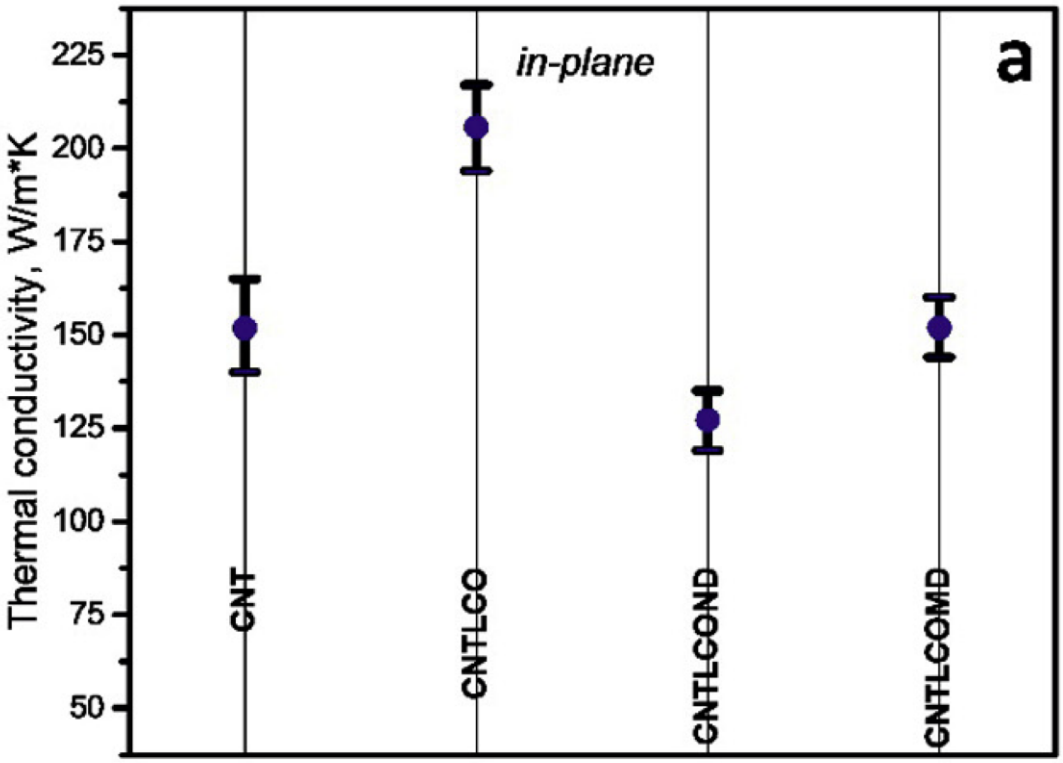

Figure 3.3: Room temperature in – plane thermal conductivity of carbon nanotube based cathodes. Data includes values for control CNT, CNTLCO, CNTLCOND, and CNTLCOMD structures. Reprinted with permission from E. Lee, R.A. Salgado, B. Lee, A. V. Sumant, T. Rajh, C. Johnson, A.A. Balandin, E. V. Shevchenko, "Design of lithium cobalt oxide electrodes with high thermal conductivity and electrochemical performance using carbon nanotubes and diamond particles," Carbon, Vol. 129, pp. 702-710, 2018. Copyright © 2018 Elsevier.

Figure 3.4 shows the cross – plane thermal conductivity of the cathodes as three orders of magnitude lower than its in plane value, but it was still comparable to conventional laminate electrodes (0.07 – 0.41 $Wm^{-1}K^{-1}$). Both the in – plane and cross – plane thermal conductivity of our CNTLCO electrode was significantly greater than that of the control CNT sample. The mass density and microstructure analysis of our electrode

samples did not show any correlation with their high thermal conductivity value. We believe that the highest thermal conductivity values achieved by the CNTLCO electrode results from a lower disorder and a better coupling between the CNTs and $LiCoO_2$ particles.

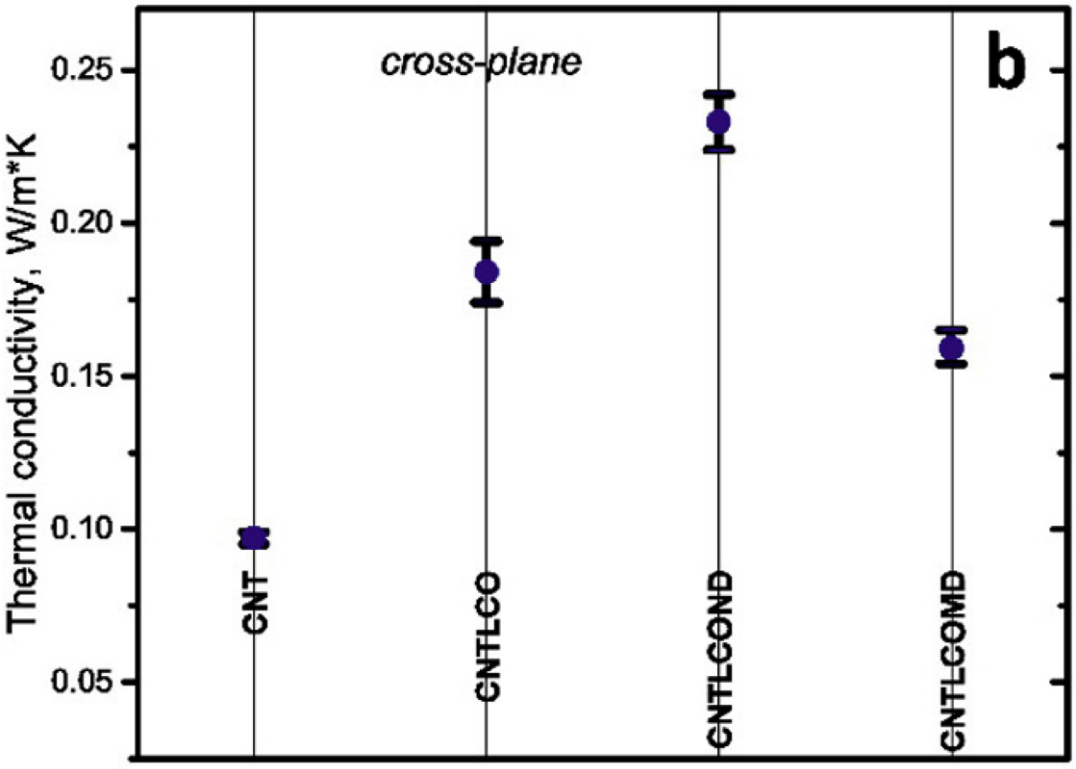

Figure 3.4: Room temperature cross – plane thermal conductivity of carbon nanotube based cathodes. Data includes values for control CNT, CNTLCO, CNTLCOND, and CNTLCOMD structures. Reprinted with permission from E. Lee, R.A. Salgado, B. Lee, A. V. Sumant, T. Rajh, C. Johnson, A.A. Balandin, E. V. Shevchenko, "Design of lithium cobalt oxide electrodes with high thermal conductivity and electrochemical performance using carbon nanotubes and diamond particles," Carbon, Vol. 129, pp. 702-710, 2018. Copyright © 2018 Elsevier.

3.4 Analysis of Thermal Data

We investigated the nano and micron sized diamond particles' effect on the thermal conductivity of CNT–based electrodes. Two CNT – based electrodes were fabricated using micron and nano sized diamonds separately and labeled CNTLCOMD and CNTLCOND, respectfully. Equal amounts of micron and nano sized diamond particle were separately introduced to fabricate each electrode. The results showed that the in – plane thermal conductivity values of CNTLCOMD and CNTLCOND electrodes were lower than that of the CNTLCO electrode. The reduction of the in – plane thermal conductivity in the diamond containing samples can be a result of additional scattering of phonons propagating in individual CNTs near attached diamond particles. An improvement of cross – plane thermal conductivity in CNTLCOND over CNTLCO was observed and explained by superior coupling between the CNTs and nano sized diamonds in the cross – plane direction. The cross – plane thermal conductivity of the electrode sample fabricated with long CNTs (100 microns) was measured to be significantly lower the that of previously reported CNT–based electrodes assembled using polydisperse CNTs [23]. This can be attributed to the more pronounced lateral stacking arrangement of longer CNTs. These results showed that the arrangement of CNTs and their alignment are important factors in determining thermal conductivity. More work must be done to optimize the size of diamond particles used in electrodes to improve the coupling to other electrode material and the overall thermal conductivity.

The scanning electron microscopy (SEM) micrograph reveals the entangle CNT arrays and random orientation around lateral planes. It's important to note, however, that the majority of CNTs were aligned in a preferred in – plane orientation, as seen in Figure 3.5. The individual CNTs were mainly aligned parallel to the fiber glass filter. Small – angle X – ray scattering (SAXS) was used to characterize the morphology of the CNT based cathodes. As shown in Figure 3.6, The SAXS data revealed that the average diameter of the multi walled carbon nanotubes was around 12 nm, and the radius of the incorporated nano diamonds in sample CNTLCOND is roughly 2.3 nm. The scattering from micro sized diamonds embedded in sample CNTLCOMD was not noticeable in the SAXS data which suggests that the concentration of CNTs and LCO particles overwhelmingly exceeds that of micro size diamonds. In all structures, there were no structure factor which implies that the CNTs were separated and not bundled together, as observed in the SEM micrograph in Figure 3.5

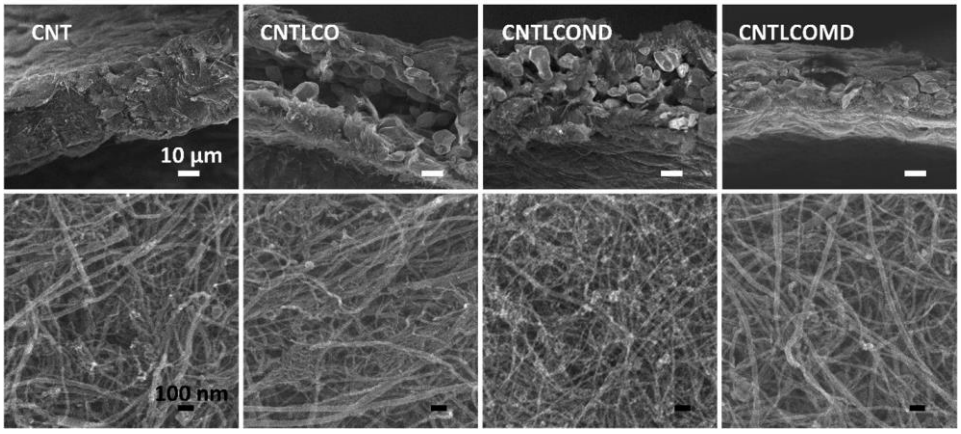

Figure 3.5: SEM micrographs of the cross section (top) and lateral plane (bottom) of reference CNT and composite CNT-LCO, CNT-LCO-ND and CNT-LCO-MD Cathodes. Reprinted with permission from E. Lee, R.A. Salgado, B. Lee, A. V. Sumant, T. Rajh, C. Johnson, A.A. Balandin, E. V. Shevchenko, "Design of lithium cobalt oxide electrodes with high thermal conductivity and electrochemical performance using carbon nanotubes and diamond particles," Carbon, Vol. 129, pp. 702-710, 2018. Copyright © 2018 Elsevier.

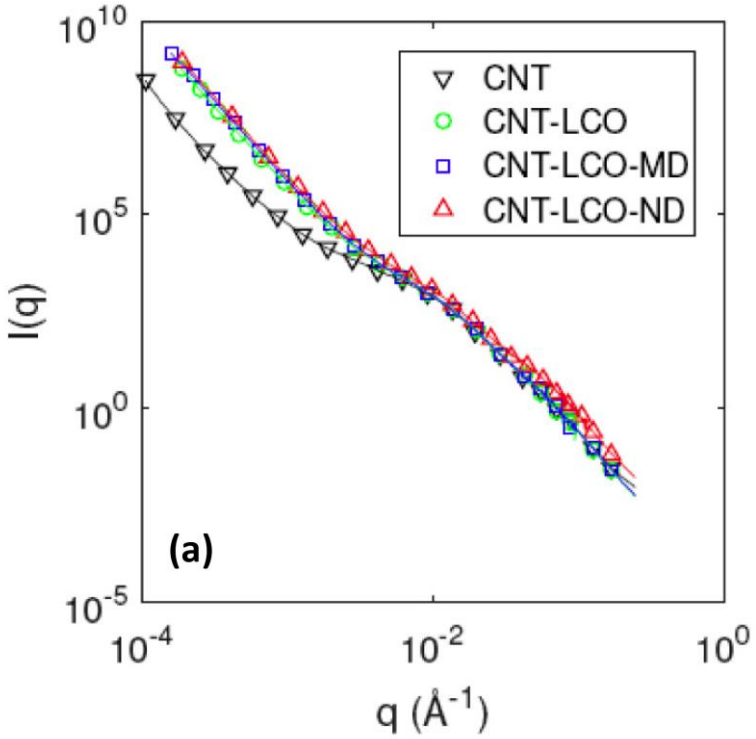

Figure 3.6: SAXS patterns measured from CNT, CNTLCO, CNTLCOND, an CNTLMD cathode structures. Reprinted with permission from E. Lee, R.A. Salgado, B. Lee, A. V. Sumant, T. Rajh, C. Johnson, A.A. Balandin, E. V. Shevchenko, "Design of lithium cobalt oxide electrodes with high thermal conductivity and electrochemical performance using carbon nanotubes and diamond particles," Carbon, Vol. 129, pp. 702-710, 2018. Copyright © 2018 Elsevier.

3.5 Electrochemical Performance of CNT Cathodes

This section is based on data reported in Ref [22]. The electrochemical testing was conducted in the Argonne National Laboratory. After the electrochemical tests, the samples were transferred to the University of California – Riverside for thermal testing. Electrochemical tests on all fabricated cathodes were taken immediately after annealing.

CNT based cathodes were cut into 1.27 cm diameter circles for electrochemical tests. Battery cycling was performed using 2032 type coin cells with a Lithium metal foil acting as a counter electrode, and a 2M lithium hexafluorophosphate ($LiPF_6$) in ethylene carbonate/ethyl methyl carbonate (3:7 weight ratio) electrolyte from Tomiyama. Half–cell cycles were operated at a 0.5 C rate. A Maccor 2000 battery tester was used while all coin cells were tested in an environment chamber at 25° C. As shown in Figure 3.7, all cathodes demonstrated similar electrochemical stability between the cycling range 2.75–4.5 Volts (V), with LCO performing the best. The CNT based cathodes modified with either nano or micro sized diamond particles, showed a decay in performance. Cycling voltage above 4.1 V is known to promote electrochemical oxidation of the organic electrolyte, which leads to the growth of a thick passivation layer at the interface of the cathode [24]. The lower stability of the cathodes modified with diamond particles, cycled at high voltage (> 4.1V), can be due to the reduced contact area between LCO particles and CNTs, as the diamond particles adhere to the CNTs' surface.

The overall, reduced performance of CNT based cathodes modified with either nano or micro sized diamond particles can be attributed by their higher porosity. Increased porosity of these cathodes can lead to an accelerated degradation of the active LCO material. The assumption here is that the LCO particles have an increased electrical connection with the CNTs in the CNTLCO cathodes, resulting in an enhanced electrical current distribution and less locally overcharged regions on the cathode. Nonetheless, the capacity retention of the fabricated CNTLCO cathodes is comparable to that of optimized LCO laminated cathodes [25–27].

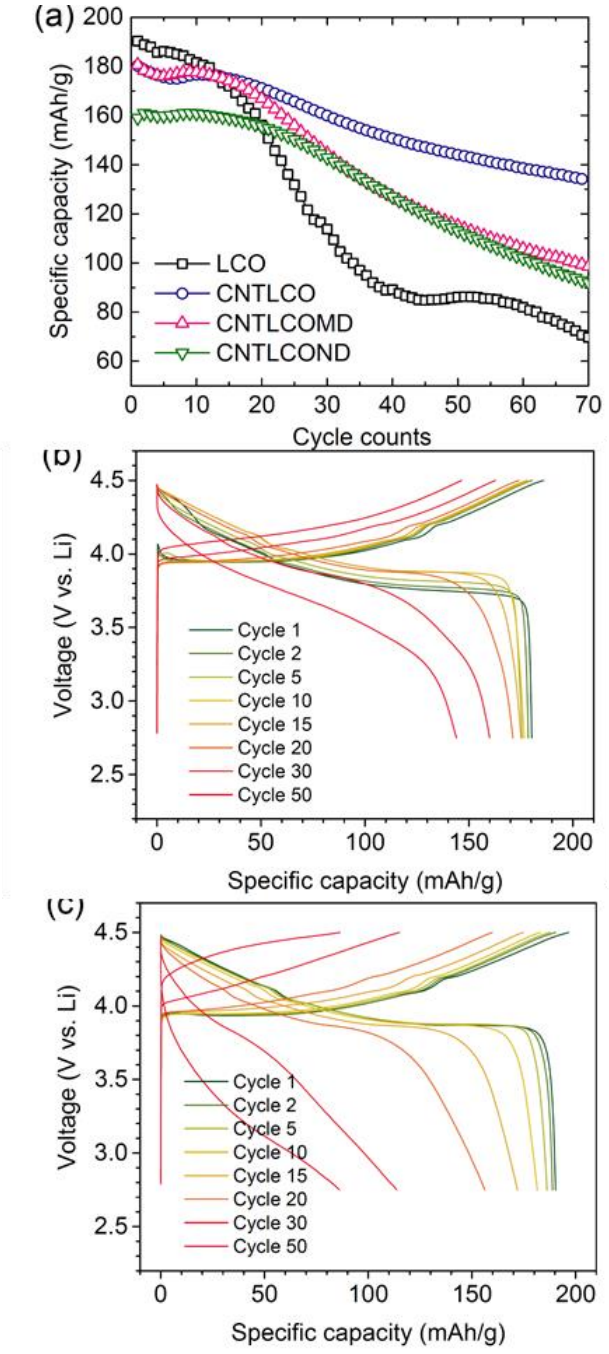

Figure 3.7: The electrochemical performance of conventional cathodes (LCO) and CNT based cathodes, cycled between 2.75 and 4.5 V at 0.5 C rate (70 mA/g): (a) cycle performance, and voltage profiles. Reprinted with permission from E. Lee, R.A. Salgado, B. Lee, A. V. Sumant, T. Rajh, C. Johnson, A.A. Balandin, E. V. Shevchenko, "Design of lithium cobalt oxide electrodes with high thermal conductivity and electrochemical performance using carbon nanotubes and diamond particles," Carbon, Vol. 129, pp. 702-710, 2018. Copyright © 2018 Elsevier.

3.6 References

[1] Whittingham, M. S., “Electrical Energy Storage and Intercalation Chemistry,” *Science,* vol. 192, pp. 1126–1127, 1976.

[2] Nitta, N., Wu, F., Lee, J. T., and Yushin, G., “Li–Ion Battery Materials: Present and Future,” *Materials Today,* vol. 18, pp. 252–264, 2015.

[3] Lu, L., Han, X., Li, J., Hua, J., and Ouyang, M., “A Review on the Key Issues for Lithium–Ion Battery Management in Electric Vehicles,” *Journal of Power Sources*, vol. 226, pp. 272–288, 2013.

[4] Goodenough, J. B. and Park, K.–S., “The Li–Ion Rechargeable Battery: A Perspective,” *J. Am. Chem. Soc.*, vol. 135, pp. 1167–1176, 2013.

[5] Etacheri, V., Marom, R., Elazari, R., Salitra, G., and Aurbach, D., “Challenges in the Development of Advanced Li–Ion Batteries: A Review,” *Energy and Environmental Science*, vol. 4, pp. 3243–3262, 2011.

[6] Dunn, B., Kamath, H., and Tarascon, J. M., “Electrical Energy Storage for the Grid: A Battery of Choices,” *Science,* vol. 334, pp. 928–935, 2011.

[7] Burheim, O. S., Onsrud, M. A., Pharoah, J. G., Vullum–Bruer, F., and Vie, P. J. S., “Thermal Conductivity, Heat Sources and Temperature Profiles of Li–Ion Batteries,” *ECS Trans.*, vol. 58, pp. 145–171, 2014.

[8] Linden, D. and Reddy, T. B., "*Handbook of Batteries"*, McGraw–Hill Professional, New York, Third Edition, 2002.

[9] Spotnitz, R. and Franklin, J., “Abuse Behavior of High–Power, Lithium–Ion Cells,” *J. Power Sources,* vol. 113, pp. 81–100, 2003.

[10] Vetter, J., Novák, P., Wagner, M. R., Veit, C., Moller, K. C., Besenhard, J. O., Winter, M., Wohlfahrt–Mehrens, M., Vogler, C., and Hammouche, A., "Ageing Mechanisms in Lithium–Ion Batteries," *J. Power Sources*, vol. 147, 269–281, 2005.

[11] Bandhauer, T. M., Garimella, S., and Fuller, T. F., "A Critical Review of Thermal Issues in Lithium–Ion Batteries," *J. Electrochem. Soc.*, vol. 158, R1–R25, 2011.

[12] Ramadass, P., Haran, B., Gomadam, P. M., White, R., and Popov, B. N., "Development of First Principles Capacity Fade Model for Li–Ion Cells," *J. Electrochem. Soc.*, vol. 151, A196–A203, 2004.

[13] Vishwakarma, V., Waghela, C., Wei, Z., Prasher, R., Nagpure, S. C., Li, J., Liu, F., Daniel, C., and Jain, A., "Heat Transfer Enhancement in a Lithium–Ion Cell through Improved Material–Level Thermal Transport," *J. Power Sources*, vol. 300, pp. 123–131, 2015.

[14] Su, F.–Y., Dai, L.–Q., Guo, X.–Q., Xie, L.–J., Sun, G.–H., and Chen, C.–M., "Micro–Structure Evolution and Control of Lithium–Ion Battery Electrode Laminate," *J. Energy Storage*, vol. 14, pp. 82–93, 2017.

[15] Maleki, H., Hallaj, S. Al, Selman, J. R., Dinwiddie, R. B., and Wang, H., "Thermal Properties of Lithium-Ion Battery and Components," *J. Electrochem. Soc.* , vol. 146, pp. 947–954, 1999.

[16] Nanda, J., Martha, S. K., Porter, W. D., Wang, H., Dudney, N. J., Radin, M. D., and Siegel, D. J., "Thermophysical Properties of $LiFePO_4$ Cathodes with Carbonized Pitch Coatings and Organic Binders: Experiments and First–Principles Modeling," *J. Power Sources*, vol. 251, pp. 8–13, 2014.

[17] Gotcu, P. and Seifert, H. J., "Thermophysical Properties of $LiCoO_2$–$LiMn_2O_4$ Blended Electrode Materials for Li–Ion Batteries," *Phys. Chem. Chem. Phys.*, vol. 18, pp. 10550–10562, 2016.

[18] Balandin, A. A., "Thermal Properties of Graphene and Nanostructured Carbon Materials," *Nat. Mater.*, vol. 10, pp. 569–581, 2011.

[19] Balandin, A. A., Ghosh, S., Bao, W., Calizo, I., Teweldebrhan, D., Miao, F., and Lau, C. N., "Superior Thermal Conductivity of Single–Layer Graphene," *Nano Lett.*, vol. 8, pp. 902–907, 2008.

[20] Eda, G., Fanchini, G., and Chhowalla, M., "Large–Area Ultrathin Films of Reduced Graphene Oxide as a Transparent and Flexible Electronic Material," *Nat. Nanotechnol.*, vol. 3, 270, 2008.

[21] Hone, J., Whitney, M., Piskoti, C., and Zettl, A., "Thermal Conductivity of Single–Walled Carbon Nanotubes," *Phys. Rev. B*, vol. 59, pp. R2514–R2516, 1999.

[22] Lee, E., Salgado, R. A., Lee, B., Sumant, A. V., Rajh, T., Johnson, C., Balandin, A. A., and Shevchenko, E. V., "Design of Lithium Cobalt Oxide Electrodes with High Thermal Conductivity and Electrochemical Performance Using Carbon Nanotubes and Diamond Particles," *Carbon*, vol. 129, pp. 702–710, 2018.

[23] Koo, B., Goli, P., Sumant, A. V, dos Santos Claro, P. C., Rajh, T., Johnson, C. S., Balandin, A. A., and Shevchenko, E. V, "Toward Lithium Ion Batteries with Enhanced Thermal Conductivity," *ACS Nano*, vol. 8, pp. 7202–7207, 2014.

[24] Choi, S. S. and Lim, H. S., "Factors That Affect Cycle–Life and Possible Degradation Mechanisms of a Li–Ion Cell Based on $LiCoO_2$," *J. Power Sources*, vol. 111, pp. 130–136, 2002.

[25] Jo, M., Jeong, S., and Cho, J., "High Power $LiCoO_2$ Cathode Materials with Ultra Energy Density for Li–Ion Cells," *Electrochem. commun.*, vol. 12, pp. 992–995, 2010.

[26] Cho, J., Kim, Y. J., and Park, B., "Novel $LiCoO_2$ Cathode Material with Al_2O_3 Coating for a Li Ion Cell," *Chem. Mater.*, vol. 12, pp. 3788–3791, 2000.

[27] Chen, Z. and Dahn, J. R., "Effect of a ZrO_2 Coating on the Structure and Electrochemistry of $LixCoO_2$ When Cycled to 4.5 V," *Electrochem. Solid–State Lett.*, vol. 5, pp. A213–A216, 2002.

Chapter 4

4 Low – Dimensional van der Waals Materials

4.1 Van der Waals Materials

Van der Waals materials can be imagined as stacked layers of covalently or ionic bonded atoms which can be visualized a two – dimensional plane (2D). Their name was given in honor of the 1910 Nobel prize winner in Physics, Johannes Diderik van der Waals, who worked on intermolecular forces and equations of state. Van der Waals materials are layered materials that have strong covalent in–plane bonds but weak inter layer van der Waals bonds [1]. It is this weak inter layer bonding which allows individual van der Waals layers to easily slide relative to each other, providing low friction properties. These properties have enabled van der Waals Materials to be readily used as dry lubricant materials. A table of traditional van der Waals materials and their application can be seen in Table 4.1 [2].

Table 4.1; Heavily studied van der Waals materials and their applications

Materials	Application
Molybdenum Disulfide (MoS_2)	Automobile lubricant
Tungsten Diselenide (WSe_2)	High end bearing lubricant
Hexagonal Boron Nitride (h-BN)	Space application lubricant
Graphite	Food industry lubricant

It was previously believed that van der Waals materials could not exist as individual layers because it was believed to be thermodynamically unfavorable. This belief was disproven when Andre Geim and Konstantin Novoselov discovered that Graphite could be separated into individual atomic layers known as graphene by means of physical exfoliation using scotch tape [3]. As seen in Figure 4.1, the exfoliation of graphite demonstrated that a 2D atomic plane of carbon atoms could exist. This discovery unveiled the spectacular properties of graphene and sparked interest in exfoliating and isolating other van der Waals materials into atomic layers which would lead to a new field of study known as 2D materials.

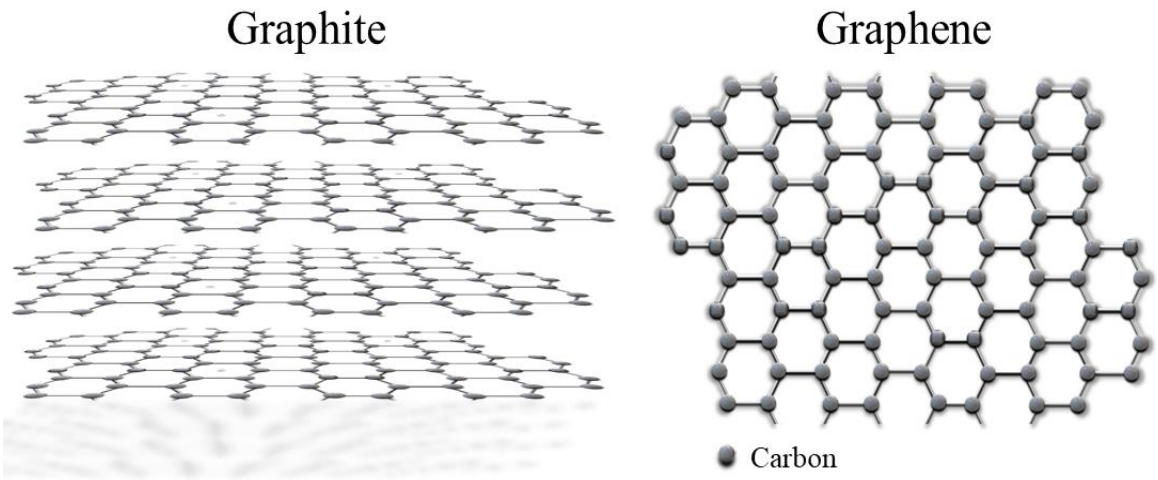

Figure 4.1: The schematic on the left depicts graphite as made up of single stacked layers of carbon planes. As depicted on the schematic on the right, graphene is a single atomic plane consisting of in – plane,covalently bonded carbon atoms.

Since graphene's discovery, there have been numerous studies on the intrinsic properties of 2D materials exfoliated from many commonly known van der Waals material

systems including those listed in Table 4.1. Consequently, many of the low hanging fruits have been plucked and studied [4]. Nevertheless, there remains several interesting van der Waals 2D and 1D material systems which exhibit exotic behavior under applied stimuli such as the charge density wave effect.

4.2 Low – Dimensional van der Waals Materials

Graphene's discovery in 2004, reinvigorated the nanoscience community and sparked a new interest in the exploration of other 2D Materials. The intrigue in finding exotic electronic and opto–electronic properties led many researchers to publish over 10,000 scientific papers on the subject annually [5]. The number of papers dedicated to graphene is expected to dwindle down as the attention is shifted to other exotic van der Waals materials that can be exfoliated to few and even mono 2D layers. The number of potential van der Waals materials that can be easily cleaved to low – dimensional is ever – growing. The melting temperature of several of these materials decreases with decreasing thickness which leads to natural passivation of their surface. Consequently, many of these proposed 2D materials will not survive at ambient temperatures as they would readily corrode and decompose.

Table 4.2: Heavily Studied low – dimensional layered materials

Group IV	Graphene C, Silicene Si, Germanane, GeH
Dichalcogenides	$FeSe_2$, PtS_2, WTe_2, MoS_2, NbS_2
Trichalcogenides	Bi_2Se_3, Sb_2Te_3, $ZrTe_3$, $NbSe_3$
Halides	MoO_3, WO_3, TaO_3
Oxides	ZrBr, CdI_2, $CoCl_2$, $RuCl_3$

.

Of the layered materials that can survive in ambient temperature, many can be classified as what are known as transition metal dichalcogenides (TMDs). These layered transition–metal dichalcogenides with the formula MX_2 where M is a transition metal such as Mo, W, Nb, Ta or Ti and X is a chalcogenide element such as Se, S or Te. Some of these materials exhibit the intriguing CDW phase transitions where their electronic properties switch from metallic to insulating as temperature decreases. Another class of the transition metal chalcogenides, the trichalcogenides, exhibits quasi – 1D crystalline structures. Examples of such materials can be found in Table 4.2 and include materials such as Sb_2Te_3 and $ZrTe_3$ [6–10]. In this Chapter, 2D TMD 1*T* –TaS_2 will be studied as it is one of the richest in terms of CDW phase change transitions with one such transition occurring near room temperature.

4.3 1*T* – Tantalum Disulfide

The charge – density – wave (CDW) phase is a macroscopic quantum state consisting of a periodic modulation of the electronic charge density accompanied by a periodic distortion of the atomic lattice in quasi – 1D or layered 2D metallic crystals [11]. Several layered transition metal dichalcogenides (TMD), including 1*T*–TaS_2 exhibit unusually high transition temperatures to different CDW symmetry – reducing phases [11]. Tantalum disulfide is composed of TaS_2 atomic planes which consist of tantalum atoms in between sulfur atoms bonded by strong covalent bonds and weak inter – layer van der Waals bonds that can be broken to isolate individual layers. The material reveals itself as a metallic crystal. As the material is thinned down it takes on a yellowish color and at a few nanometers in thickness it takes on a blue tint. Previous investigations in TaS_2 focused on two known phases, named as 1*T* and 2H [13]. In the 2H phase, sulfur atoms are ordered around tantalum atoms in a trigonal prismatic order, while in the 1*T* phase, sulfurs atoms surround tantalum atoms at the corners of an octahedron, as illustrated in Figure 4.2 a) and (b). The 1*T* polytype of TaS_2 undergoes the transition from a normal metallic phase to an incommensurate CDW (IC – CDW) phase at 545 K, then to a nearly – commensurate CDW (NC–CDW) phase at 350 K, and, finally, to a commensurate CDW (C – CDW) phase at 180 K [12]. Each phase transition is accompanied by a lattice reconstruction and a change in electrical resistivity. As the materials becomes more electrically conductive as it transitions from its C – CDW phase to the IC – CDW metallic phase. Figure 4 c) shows

the signature formation of a “David star” in the C – CDW phase, as 12 Tantalum atoms move inward toward a central Tantalum atom.

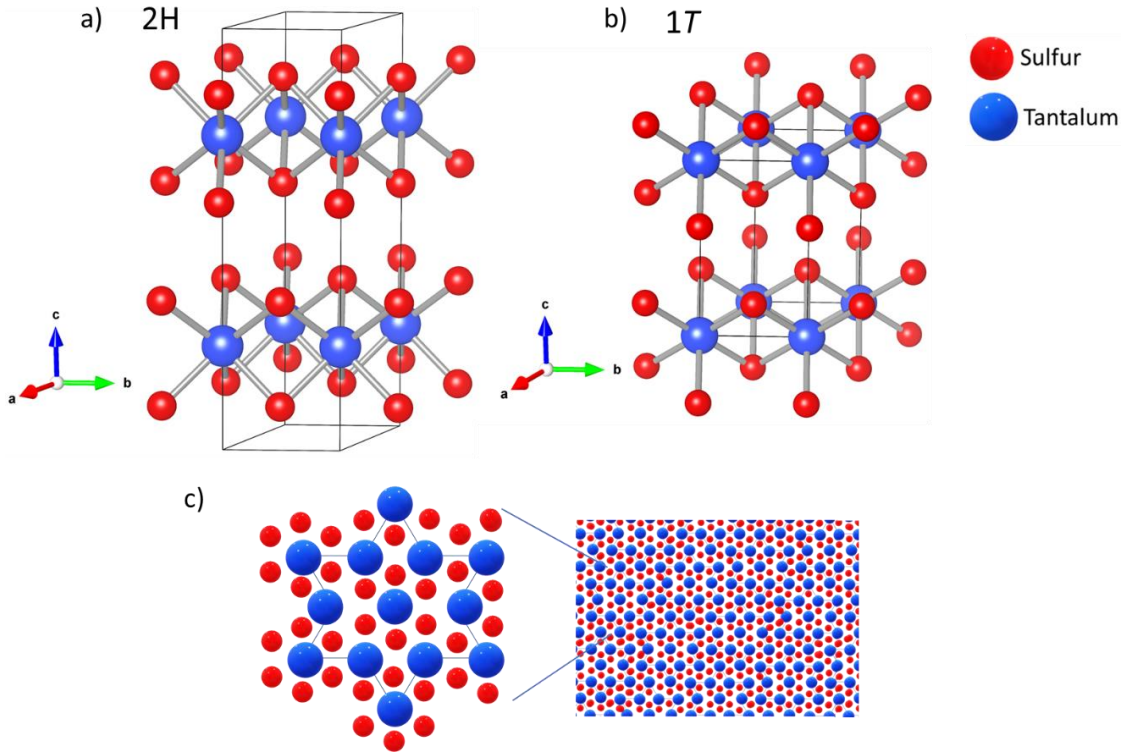

Figure 4.2: A schematic representation of a) 2H – TaS_2 unit cell, b) the 1*T* – TaS_2 unit cell, and c) the signature “star of David” clusters observed in the commensurate phase.

4.4 Material Synthesis

1*T* – TaS_2 crystals were synthesized using the chemical vapor transport (CVT) method from high purity elemental powders. The metastable 1*T* phase, found in high temperatures, was isolated by quenching the reaction in ice to produce metallic crystals. The crystals were

analyzed by powder X–ray diffraction. The results, shown in Figure 4.3, reveal a pure phase product that matched the 1*T* phase (ICDD 04–006–1132). A strong orientation effect is measured which is attributed to the layered structure seen in the insert of Figure 4.3 a). Figure 4.3 b) shows a SEM micrograph which demonstrates the millimeter size of high quality 1*T* – TaS_2 crystal grown via the CVT method. Figure 4.3 c) shows the results of energy dispersive spectroscopy (EDS) measurements which show that the stoichiometric ratio between tantalum and sulfur is 1 to 2. Additionally, electron probe microanalysis (EPMA) results revealed a tantalum to sulfur stoichiometric ratio of 1 to 2.1, which is close to an ideal stoichiometry. More information on the CVT synthesis and details on the control of polytype formation can be found in previous studies [15–18].

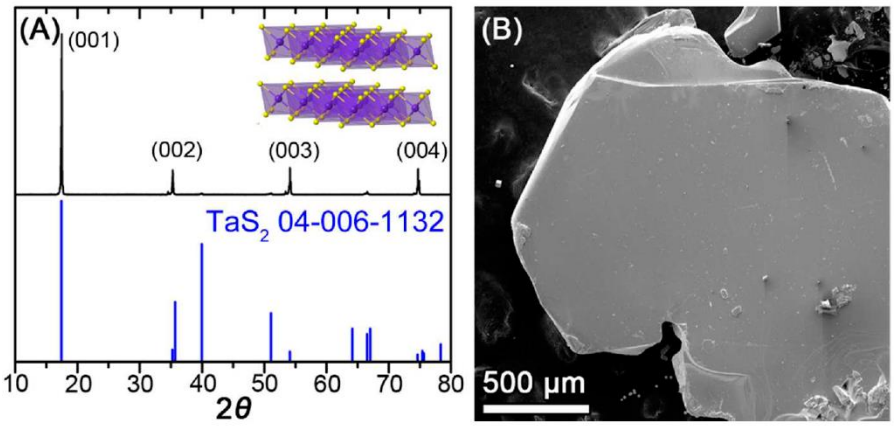

(C)

	EDS (at. %)	EPMA (at. %)
Ta	33.3	31.84
S	66.7	68.12

Figure 4.3: A) Results of powder X – ray diffraction of CVT synthesized 1*T* – TaS_2 crystals B) An SEM image of the bulk 1*T* – TaS_2 crystals. C) A table summarizing the results of EDS and EPMA measurements which confirm the expected 1 to 2 tantalum to sulfur ratio. Reprinted with permission from G. Liu, S. Rumyantsev, M. A. Bloodgood, T. T. Salguero, and A. A. Balandin, "Low – Frequency Current Fluctuations and Sliding of the Charge Density Waves in Two – Dimensional Materials," *Nano Lett.*, vol. 18, pp. 3630–3636, 2018. Copyright © 2018 American Chemical Society.

4.5 Exfoliation of Low – Dimensional Materials

In 2004, it was discovered that graphene could be mechanically peeled off of bulk crystals of graphite using scotch tape. The exfoliation of low van der Waals materials from their constituted bulk crystal known as micro – mechanical exfoliation, can be seen in Figure 4.4. While this method does not require sophisticated and expensive equipment, there have been improvements in the quality of adhesive tape used to cleave layered materials and many have discovered that these same materials can be exfoliated by means of ultrasonication.

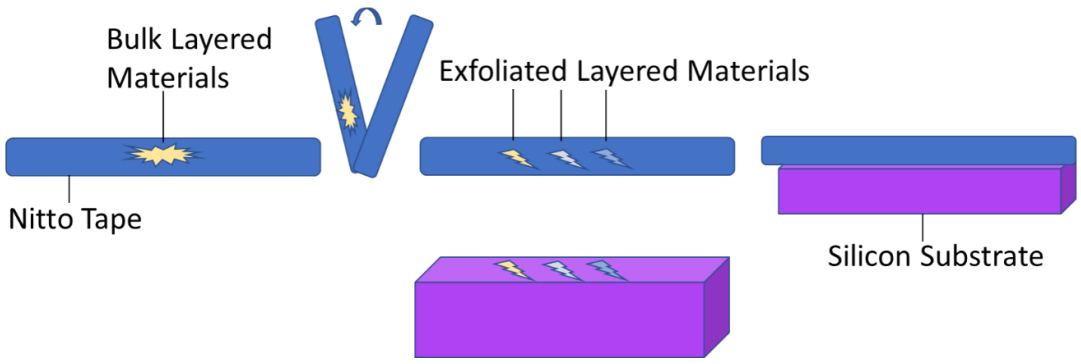

Figure 4.4: Schematic depicting the micro – mechanical exfoliation of layered materials and their transfer on to a silicon substrate.

In this dissertation, the mechanical exfoliation was solely used to produce 2D structures from bulk layered van der Waals materials. The micro – mechanical exfoliation of van der Waals materials begins by placing a bulk crystal of the studied materials on the adhesive side of a low residue Nitto tape. Once the bulk material is secured on the adhesive

tape, the adhesive tape is folded so that all adhesive surfaces come into contacted with each other. The tape is then removed, and the exfoliated materials are transferred onto the Si/SiO_2 substrate. The exfoliated material was then transferred on to a Si/SiO_2 substrate by pressing the Nitto tape onto the target substrate and gently rubbing for a few minutes. The tape is then removed, and the exfoliated materials are transferred onto the Si/SiO_2 substrate, as seen in Figure 4.5. The low – dimensionality of the exfoliated layered materials is confirmed using atomic force microscopy (AFM).

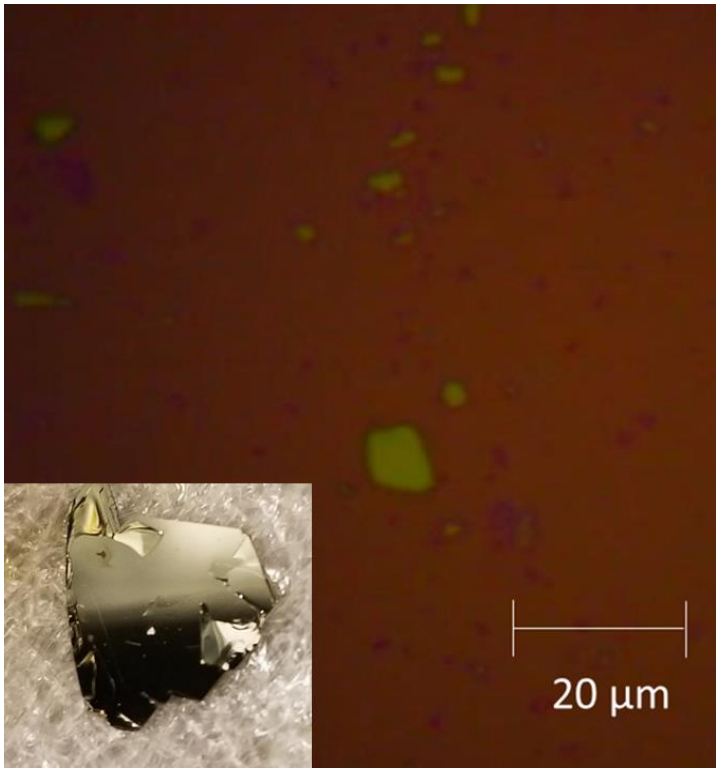

Figure 4.5: Optical image showing exfoliated thin layers of 1*T* – TaS_2 on a SiO_2 substrate. The lateral dimensions were in the micrometer range while the typical thickness was under 100 nm. The insert shows a photograph of a bulk 1*T* – TaS_2 crystal.

The Raman spectroscopy is a characterization technique to identify materials based on the vibrational information of their specific chemical bonds and crystallographic symmetry. An investigated solid material possesses characteristic phonon modes that are used to identify it. Raman spectroscopy has also been used to detect the phase transition temperature in CDW materials as they undergo structural crystallographic transformation [18–21]. This technique has also been widely used as a powerful metrology tool to determine the thickness of two – dimensional materials [22–25]. Raman spectroscopy was performed on 90 nm thick 1*T* – TaS_2 material with the confocal Renishaw in – Vio system in the back – scattering mode configuration. The spatial resolution of this system was limited by the laser spot diameter which was measured to be around 1 μm. This resolution enabled us to focus on sample areas of a few microns. The sample was placed on a remotely controlled translational stage which could be coarsely moved along the x and y plane. A white light source and CCD camera was used to illuminate and focus on the sample. A laser wavelength of 633 nm was focused on the sample through a lens with a 100X magnification to excite Raman active signals. The Raman scattered, and Rayleigh light was collected using the backscattering configuration through the objective lens. Figure 4.6 shows a measured Raman spectrum of a 90 nm thick 1*T* – TaS_2 thin film. The peaks observed at 239, 302, 381 cm^{-1} correspond to the well–known optical phonon branches where sulfur atoms are involved in the atomic vibration [26].

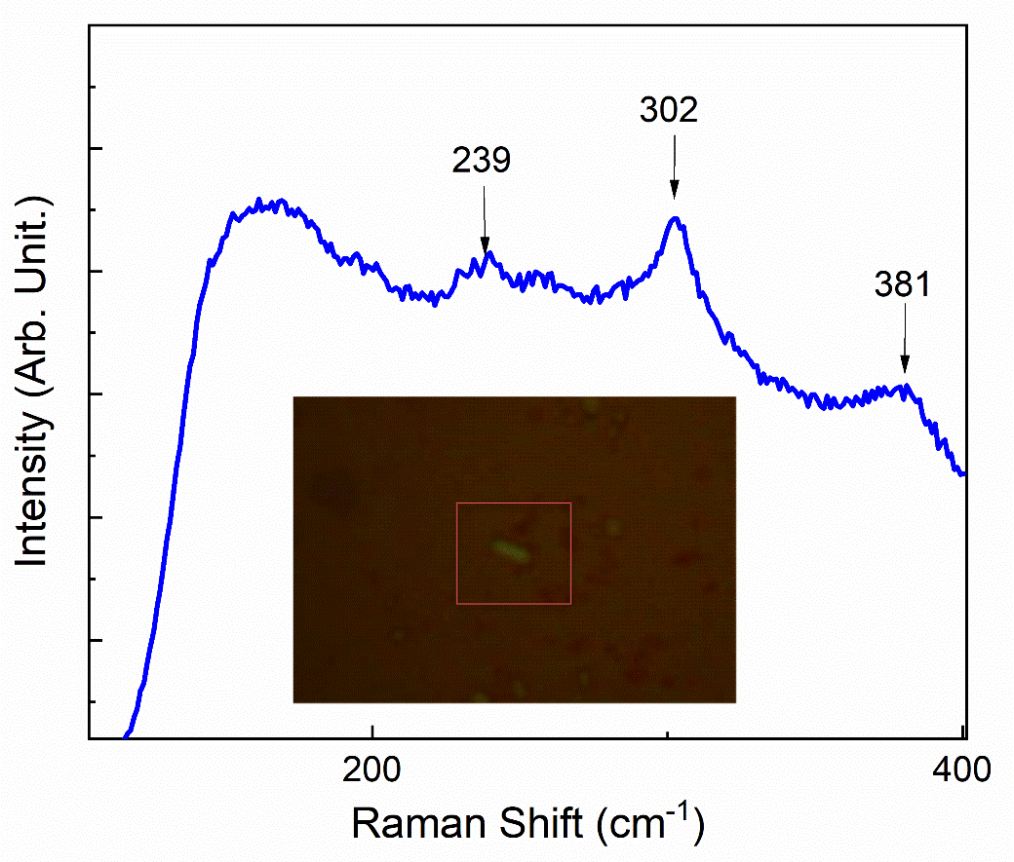

Figure 4.6: Raman spectrum of a 1*T* – TaS_2 thin film. The insert image shows an optical image of the 90 nm thick flake.

4.6 References

[1] Duong, D. L., Yun, S. J., and Lee, Y. H., "Van der Waals Layered Materials: Opportunities and Challenges," *ACS Nano*., vol. 12, pp. 11803–11830, 2017.

[2] Santner, E., "Corrosion Books: Lubricants and Lubrication. By T. Mang, W. Dresel," *Mater. Corros.*, vol. 52, 947, 2002.

[3] Novoselov, K. S., Geim, A. K., Morozov, S. V., Jiang, D., Zhang, Y., Dubonos, S. V., Grigorieva, I. V., and Firsov, A. A., "Electric Field in Atomically Thin Carbon Films," *Science.*, vol. 306, pp. 666–669, 2004.

[4] Miró, P., Audiffred, M., and Heine, T., "An Atlas of Two – Dimensional Materials," *Chemical Society Reviews*. vol. 43, pp. 6537–6554, 2014.

[5] Geim, A. K. and Grigorieva, I. V, "Van der Waals Heterostructures.," *Nature*, vol. 499, pp. 419–425, 2013.

[6] Wilson, J. A., Di Salvo, F. J., and Mahajan, S., "Charge–Density Waves and Superlattices in the Metallic Layered Transition Metal Dichalcogenides," *Adv. Phys.*, vol. 24, pp. 117–201, 1975.

[7] Giambattista, B., Slough, C. G., McNairy, W. W., and Coleman, R. V., "Scanning Tunneling Microscopy of Atoms and Charge–Density Waves in 1T–TaS_2, 1T–$TaSe_2$, and 1T–VSe_2," *Phys. Rev. B*, vol. 41, pp. 10082–10103, 1990.

[8] Island, J. O., Biele, R., Barawi, M., Clamagirand, J. M., Ares, J. R., Sánchez, C., Van der Zant, H. S. J., Ferrer, I. J., D'Agosta, R., and Castellanos–Gomez, A., "Titanium Trisulfide (TiS3): A 2D Semiconductor with Quasi–1D Optical and Electronic Properties," *Sci. Rep.*, vol. 6, 22214, 2016.

[9] Kocan, A., "Charge Density Waves in Low – Dimensional Metals," *Mafija.Fmf.Uni–Lj.Si*, pp. 1–16, 2007.

[10] Lipatov, A., Wilson, P., Shekhirev, M., Teeter, J., Netusil, R., and Sinitskii, A., "Few–Layer Titanium Trisulfide (TiS_3) Field–Effect Transistors," *Nanoscale*, vol. 7, pp. 12291–12296, 2015.

[11] Thorne, R. E., "Charge–Density–Wave Conductors," *Phys. Today*, vol. 49, pp. 42–47, 1996.

[12] Lazar, P., Martincová, J., and Otyepka, M., "Structure, Dynamical Stability, and Electronic Properties of Phases in TaS_2 from a High–Level Quantum Mechanical Calculation," *Phys. Rev. B – Condens. Matter Mater. Phys.*, vol. 92, 224104, 2015.

[13] Tsen, A. W., Hovden, R., Wang, D., Kim, Y. D., Okamoto, J., Spoth, K. A., Liu, Y., Lu, W., Sun, Y., Hone, J. C., Kourkoutis, L. F., Kim, P., and Pasupathy, A. N., "Structure and Control of Charge Density Waves in Two – Dimensional 1T–TaS_2," *Proc. Natl. Acad. Sci.*, vol. 112, pp. 15054–15059, 2015.

[14] Yan, Z., Jiang, C., Pope, T. R., Tsang, C. F., Stickney, J. L., Goli, P., Renteria, J., Salguero, T. T., and Balandin, A. A., "Phonon and Thermal Properties of Exfoliated $TaSe_2$ Thin Films," *J. Appl. Phys.*, vol. 114, 204301, 2013.

[15] Goli, P., Khan, J., Wickramaratne, D., Lake, R. K., and Balandin, A. A., "Charge Density Waves in Exfoliated Films of van der Waals Materials: Evolution of Raman Spectrum in $TiSe_2$," *Nano Lett.*, vol. 12, pp. 5941–5945, 2012.

[16] Liu, G., Debnath, B., Pope, T. R., Salguero, T. T., Lake, R. K., and Balandin, A. A., "A Charge–Density–Wave Oscillator Based on an Integrated Tantalum Disulfide – Boron Nitride–Graphene Device Operating at Room Temperature," *Nat. Nanotechnol.*, vol. 11, pp. 845–850, 2016.

[17] Liu, G., Zhang, E. X., Liang, C. D., Bloodgood, M. A., Salguero, T. T., Fleetwood, D. M., and Balandin, A. A., "Total–Ionizing–Dose Effects on Threshold Switching in 1*T*–TaS_2 Charge Density Wave Devices," *IEEE Electron Device Lett.*, vol. 38, pp. 1724–1727, 2017.

[18] Dobal, P. S., Dixit, A., Katiyar, R. S., Yu, Z., Guo, R., and Bhalla, A. S., "Micro–Raman Scattering and Dielectric Investigations of Phase Transition Behavior in the $BaTiO_3$–$BaZrO_3$system," *J. Appl. Phys.*, vol. 89, 8085, 2001.

[19] Kreisel, J., Jadhav, P., Chaix–Pluchery, O., Varela, M., Dix, N., Sánchez, F., and Fontcuberta, J., "A Phase Transition Close to Room Temperature in $BiFeO_3$ Thin Films," *J. Phys. Condens. Matter*, vol. 23, 342202, 2011.

[20] Jiang, K., Li, W., Chen, X., Zhan, Z., Sun, L., Hu, Z., and Chu, J., "Doping Effect on the Phase Transition Temperature in Ferroelectric $SrBi_2{-}xNd_xNb_2O_9$ Layer–Structured Ceramics: A Micro–Raman Scattering Study," *J. Raman Spectrosc.*, vol. 43, pp. 583–587, 2012.

[21] Wu, Y., Ren, G., Ding, D., Shang, S., Sun, D., Zhang, G., Wang, J., Pan, S., and Yang, F., "Effects of Zr^{4+} Codoping on the $Lu_{0.8}Sc_{0.2}BO_3$:Ce Scintillation Materials," *J. Lumin.*, vol. 134, pp. 345–351, 2013.

[22] Lee, C., Yan, H., Brus, L. E., Heinz, T. F., Hone, J., and Ryu, S., "Anomalous Lattice Vibrations of Single– and Few–Layer MoS_2," *ACS Nano*, vol. 4, pp. 2695–2700, 2010.

[23] Gupta, A., Chen, G., Joshi, P., Tadigadapa, S., and Eklund, "Raman Scattering from High – Frequency Phonons in Supported n–Graphene Layer Films," *Nano Lett.*, vol. 6, pp. 2667–2673, 2006.

[24] Ferrari, A. C., Meyer, J. C., Scardaci, V., Casiraghi, C., Lazzeri, M., Mauri, F., Piscanec, S., Jiang, D., Novoselov, K. S., Roth, S., and Geim, A. K., "Raman Spectrum of Graphene and Graphene Layers," *Phys. Rev. Lett.*, vol. 97, 187401, 2006.

[25] Balandin, A. A., Ghosh, S., Bao, W., Calizo, I., Teweldebrhan, D., Miao, F., and Lau, C. N., "Superior Thermal Conductivity of Single–Layer Graphene," *Nano Lett.*, vol. 8, pp. 902–907, 2008.

[26] Duffey, J. R., Kirby, R. D., and Coleman, R. V, "Raman Scattering from 1T–TaS_2," *Solid State Commun.*, vol. 20, pp. 617–621, 1976.

Chapter 5

5 Device Fabrication and Characterization

5.1 Introduction

The approach and methodologies in this section are focused on the fabrication of two terminal vertical electrical devices based on low – dimensional van der Waals materials. A brief schematic of the important steps in the device fabrication process can be seen in Figure 5.1. The following sections will describe the electron beam lithography, electron beam evaporation, exfoliation and deterministic transfer of low – dimensional materials and the electrical characterization.

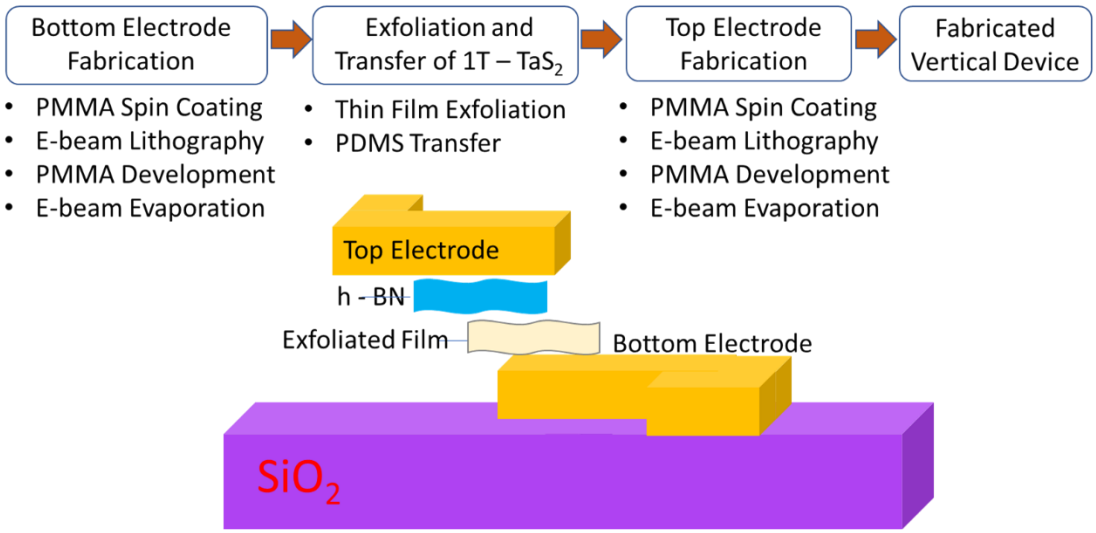

Figure 5.1: Schematic depicting the fabrication and characterization of a vertical device.

5.2 Electron Beam Lithography

Electron beam lithography (EBL) is a lithography that uses a focused electron beam to expose patterns in polymer shadow masks which will later be used to deposit or etch materials away from a target substrate. This is in contrast with the industry used photolithography which uses light to expose patterns for the same applications. EBL produces patterning with a higher resolution than photolithography because of the short wavelength of the electron bean which is in the range of 10 to 50 keV. As seen in Figure 5.2, a standard EBL system consists of the following core components: an electron gun or electron source that supplies the electrons. an electron column consisting of lenses and electrodes which conforms and focuses the electron beam, a mechanical stage that positions the wafer under the electron beam, and a computer system that controls all components [1–4].

Before electron beam lithography, a substrate (usually SiO_2 wafer) is coated with a polymer mask [5–7]. This is done by spin coating two layers of Poly (methyl methacrylate) (PMMA) at a rotation of 4000 revolutions per minute for 45 seconds. The substrate is then baked at 180°C for 10 minutes to remove any excess solvent. The substrate is then taken to SEM chamber equipped with electron beam lithography capabilities. AutoCAD software is used to design the electrode patterns which the electron beam will expose on the PMMA mask. As the electron beam traces the previously defined electrode pattern, the solubility of the exposed traced patterned is altered. The coated substrate is then submerged in a 3:1 methyl isobutyl ketone (MIBK) & Isopropanol based developer where it dissolves portions

of the PMMA mask which were exposed and patterned by an electron beam [8, 9]. The substrate is then ready for metal deposition.

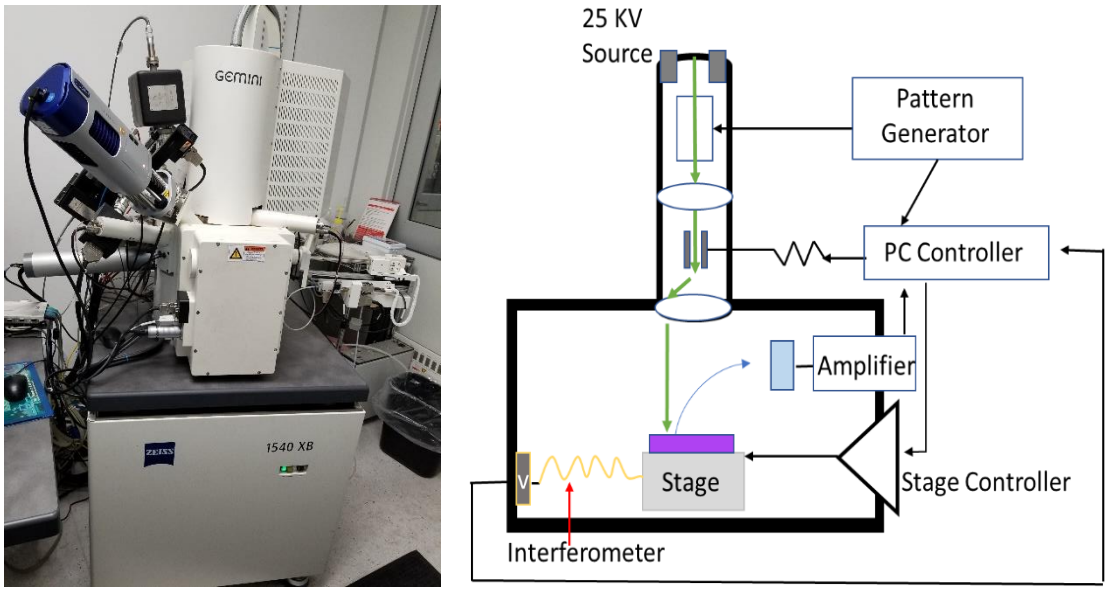

Figure 5.2: On the left, a photograph of a scanning electron microscope (SEM) equipped with an electron beam lithography system. On the right, a schematic of an electron beam lithography system illustrates the critical components. Center for Nanoscale Science and Engineering (CNSE), UC Riverside.

5.3 Electron Beam Evaporation

Electron Beam Physical Vapor Deposition or EBPVD is a form of physical vapor deposition in which a target is bombarded with an electron beam from a charged tungsten filament under ultra–high vacuum [10,11]. The electron beam causes atoms from the target material to transform into the gaseous phase. These atoms then precipitate into solid form,

coating everything in the vacuum chamber (within line of sight) with a thin layer of the bombarded material. Alternatively, in chemical vapor deposition (CVD), the film growth takes place at high temperatures, leading to the formation of corrosive gaseous products, and it may leave impurities in the substrate [12–14]. The PVD process utilized by the electron beam evaporation method can be carried out at lower deposition temperatures and without corrosive products, but deposition rates are typically lower. The deposition chamber must be evacuated to a vacuum pressure of at least 7.5×10^{-5} Torr (10^{-4} Pa) to allow electrons to travel from the electron gun to the ingot shaped evaporation material. Electron beams can be generated by thermionic emission, field electron emission or by the anodic arc method. The generated electron beam is accelerated to a high kinetic energy which is then converted into other forms of energy through interactions with the evaporation material. The thermal energy that is produced heats up the evaporated material causing it to melt or sublimate. The Accelerating voltages in electron beam evaporation can be between 3 kV – 40 kV.

The evaporation process for low – dimensional materials is typically done once for Titanium to a thickness of 10 nm followed by a gold layer of about 100 nm. The titanium layer enhances the adhesion between the deposited gold metal and the substrate. The evaporator used is the Temescal Model BJD – 1800 electron beam evaporator. A schematic representing all the critical components of the electron beam evaporator can be seen in Figure 5.3. An electron gun bombards a crucible containing the material to be evaporated and a crystal thickness monitor is used to inspect the quality and quantity of the evaporant source material. Once a metal layer is evaporated on the surface of the substrate, the

substrate is submerged in acetone to dissolve the undeveloped layers of PMMA. This results in metal patterns, previously defined by EBL, on the surface of the substrate.

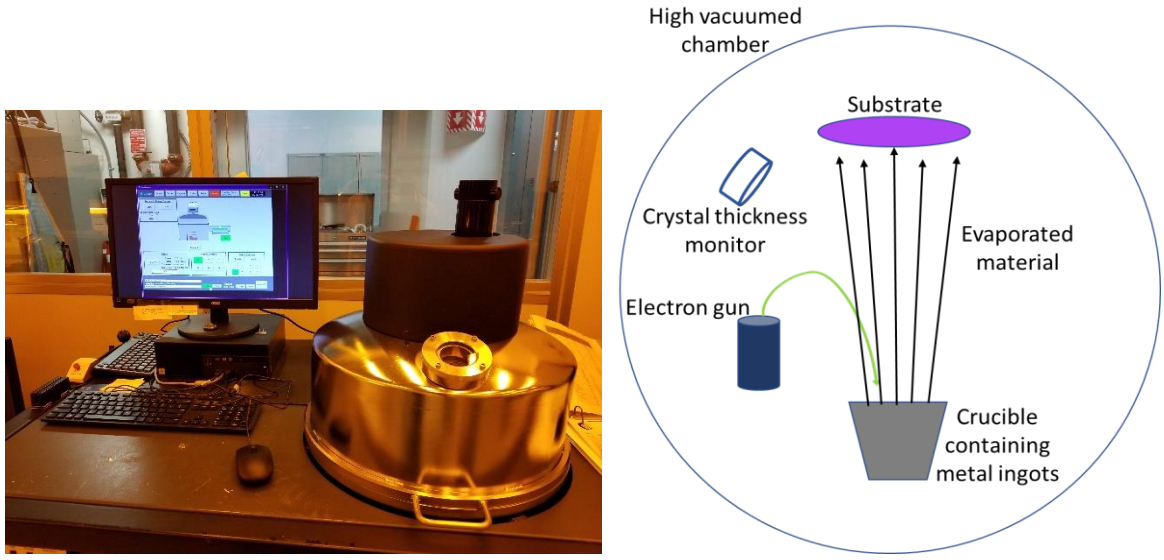

Figure 5.3: On the left, a photograph of an electron beam evaporator. On the right, a schematic representing the critical components of an electron beam evaporation chamber is shown. Adapted with permission from S. Ahmadi, N. Asim, M.A. Alghoul, F.Y. Hammadi, K. Saeedfar, N.A. Ludin, S. Zaidi, and K. Sopian, "The Role of Physical Techniques on the Preparation of Photoanodes for Dye Sensitized Solar Cells", International Journal of Photoenergy, 198734, 2014. Copyright © 2014. Center for Nanoscale Science and Engineering (CNSE), UC Riverside.

5.4 Transfer of Low – Dimensional Materials

Most methods used to transfer low – dimensional materials rely on a sacrificial polymer layer which requires the use of chemicals during the fabrication process. These chemicals

may contaminate the transferred material [15–19]. In this dissertation, an all dry transfer method was used to transfer thin layers of $1T - TaS_2$ on pre–patterned bottom electrodes. This all dry transfer method relies on the viscoelasticity of Polydimethylsiloxane (PDMS) stamps [20–22]. Figure 5.4 shows a schematic of the all dry transfer set–up. The PDMS stamp is a commercially available material (Gelfilm, Gelpak). This stamp is adhered to a glass slide for ease of handling. Two – dimensional $1T - TaS_2$ was first exfoliated on to a PDMS/glass slide in the same way shown in Figure 4.4. The surface of the PDMS stamp is placed under a microscope to select thin flakes which appear with a faint contrast. Since the PDMS stamp is transparent, the number of atomic layers on a thin flake can be determined using transmission mode. Once a suitable film is identified, a Si/SiO_2 substrate with prepatterned electrodes is affixed to a stage using carbon tape. The stamp is then attached to a three – axis manipulator with the exfoliated films facing the target substrate.

The set–up seen in Figure 5.4 is used to align a desired thin film on the pre–patterned electrodes, using the DSLR camera, zoom lens and monitor. To successfully transfer the selected thin films on the pre–patterned electrodes, the stamp is pressed on to the Si/SiO_2 , and then slowly separated. The transfer of exfoliated thin films from the PDMS stamp to the pre–patterned electrodes is possible due to the viscoelasticity of the PDMS material. As It behaves as an elastic solid while it is in contact with the targeted substrate and flows at short time intervals as it is slowly peeled away.

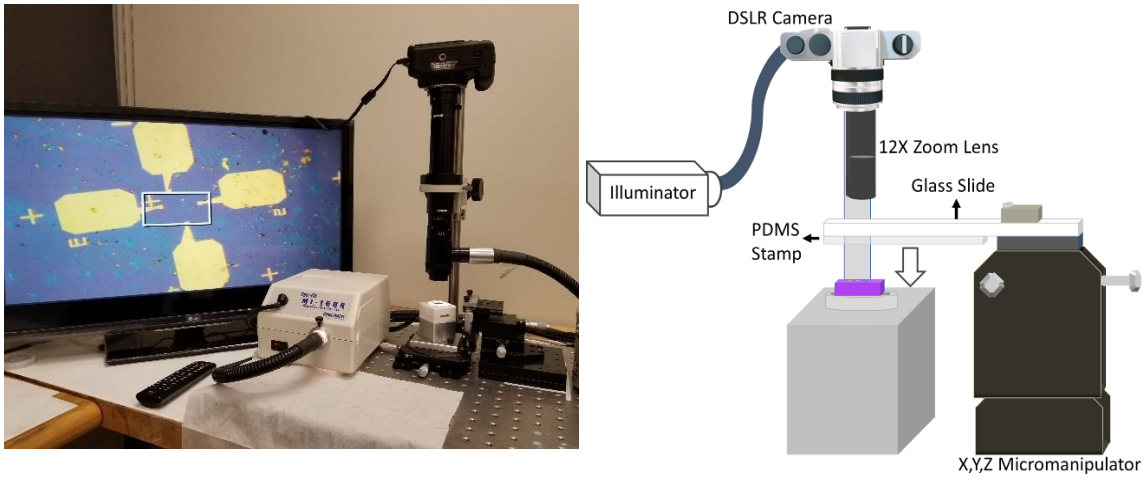

Figure 5.4: The left image shows a photograph of the all dry transfer system. On the right, a schematic is shown that illustrates the working components of an all dry transfer system used to transfer thin films of 1*T* – TaS_2 on to pre – patterned electrodes. Nano – Device Laboratory (NDL), UC Riverside.

5.5 Electrical Characterization of Devices

The vertical electrical transport of low – dimensional material can be probed by fabricating a vertical device using the techniques discussed in the previous sections and measuring its current – voltage characteristics. In this dissertation, an electrical probe station (Lakeshore TTPX), and an integrated semiconductor analyzer (Agilent Technologies B1500A) was used to probe the current – voltage characteristics of vertical devices. The vertical device is placed inside a chamber which is then vacuumed to 10^{-5} torr. Electrical probes are then placed in contact with the electrodes of the vertical devices, using an optical microscope. The electrical probes are connected to the source–measure unit (SMU) channels on the semiconductor device analyzer via coaxial cables. The semiconductor device analyzer can test the performance of electrical devices by capacitance, time dependent capacitance, and

current voltage measurements. The current measurement resolution is as low as a few femto amperes (A). The SMU channels provides both current and voltage sources, and current and voltage meters in a single compact unit. The prospect of high accuracy and low current resolution make this set–up an ideal electrical characterization tool. Figure 5.5 shows a photograph of the electrical characterization set–up.

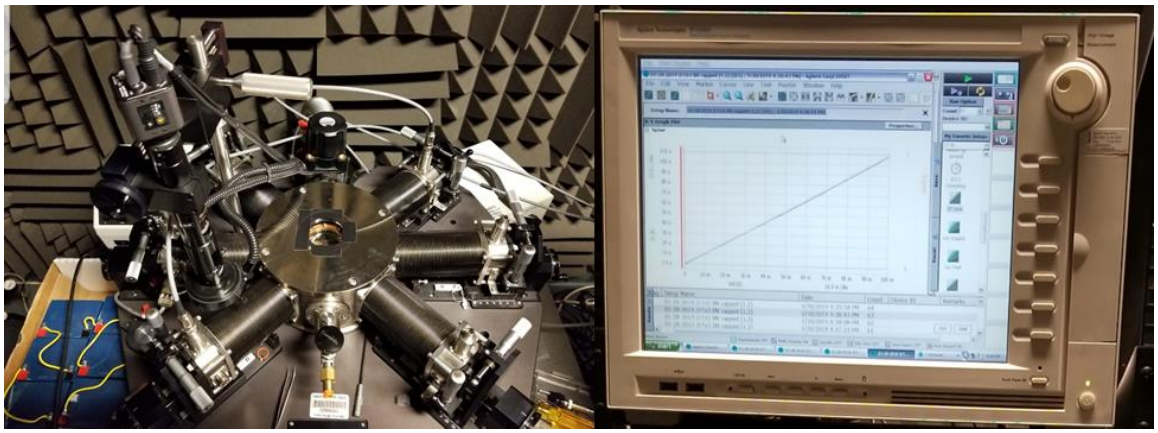

Figure 5.5: A photograph showing a six – probe Lakeshore electrical probe station (TTPX) on the left and a Agilent B1500a semiconductor device analyzer on the right. Nano – Device Laboratory (NDL), UC Riverside.

Low temperature current voltage measurements in the electrical probe station were conducted by cooling down the chamber using liquid nitrogen. The temperature in the chamber was controlled using a heater, which is adhered to the bottom of the sample stage, and temperature controller (Lakeshore 336). The temperature controller provides a stable temperature inside the vacuumed sample chamber. The controller senses the chamber temperature fluctuations and sends DC heater power to the probe station as needed, balancing the amount of heat provided by power against the temperature decrease enabled

by the liquid nitrogen. Additionally, the controller also balances its time response against that of the probe station to achieve a stable temperature without fluctuations or unnecessary delays.

5.6 Low – Frequency Electronic Noise

Electrical noise characterized by random fluctuations in electrical signals have been studied for many years. Initially, the motivation was to optimize electrical devices by reducing electrical noise. However, as previous studies demonstrated, some forms of electrical noise are unavoidable [23–25]. Electronic noise is divided into four fundamental sub bands: thermal noise or Johnson–Nyquist noise, shot noise, generation–recombination and 1/*f* noise [23]. Other forms of noise such as avalanche noise and burst noise derive from the four sub–bands. Each of these noise types have a well–defined fundamental origin, with the exception of 1/*f* noise. Electrical noise is normally characterized by its amplitude distribution, frequency spectrum and physical mechanism. The autocorrelation function is frequently used to observe the average time dependence of fluctuating variables. The power spectrum density (power distribution with respect to frequency) of a noise type can be obtained by considering the time interval ,T, of repetitions of a randomly fluctuating signal and expanding it as a Fourier series [26]. The power spectrum density is usually denoted as S_x with x being either current or voltage. In this work, we focus on intrinsic noise types by taking every precaution to avoid external sources of noise that are not intrinsic to the investigated material.

Thermal noise originates from the fluctuation of electrical charges in a material as a result of thermal motion and is expressed as [23]:

$$S_I = 4K_B TG \tag{5.1}$$

where, S_I is the current spectral density, K_B is the Boltzmann constant, T is temperature and G is electrical conductance. Shot noise results from the discrete nature of electrical charges. Its current fluctuations is defined by [23]:

$$S_I = 2q < I > \tag{5.2}$$

where q is the charge and <I> is the average value of an electric current. Generation–recombination noise emerges from the formation of trap states in semiconductor materials which leads to a variation in the number of free electrons. This fluctuation reveals itself as a spectral density expressed as [23]:

$$S_I(f) = \frac{S_o}{[1+(2\pi f\tau)^2]} \tag{5.3}$$

where S_0 is the frequency independent portion of $S_I(f)$ at a frequency less than $< (2\pi\tau)-1\ a > (2\pi\tau)^{-1}$, and τ is the time constant associated with a specific trapping state such as an ionized impurity. Low – frequency (1/*f*) noise, first discovered in vacuum tubes, is usually found at a frequency less than 100 kHz [27]. Its spectral density can be expressed as [23]:

$$S_I(f) = 1/f^{\alpha} \tag{5.4}$$

where f is frequency and $\alpha \sim 1$. Low – frequency noise is present in almost all semiconductor devices [28]. This type of current/voltage fluctuation can be measured by passing a constant current through the device and measuring the voltage fluctuations or applying a

constant potential and measuring its current fluctuations. The relation between the current (I) and voltage (V) spectral densities is expressed by [27]:

$$\frac{S_I(f)}{I^2} = \frac{S_V(f)}{V^2} \tag{5.5}$$

The physical origin of low – frequency noise is agreed to originate from the fluctuations in the number of charge carriers, electrical mobility or both [23]. In this work, we use low – frequency noise spectroscopy to investigate the electrical transport in vertical $1T - TaS_2$.

A schematic of the noise measurement setup used to measure the low – frequency current fluctuations in vertical $1T - TaS_2$ devices can be seen in Figure 5.6. A DC potential is applied on the top and bottom electrode of a vertical device using a "quiet" 6 V battery–potentiometer circuit (V_D) to minimize the 60 Hz noise and its harmonics from the electrical grid. The voltage drop across the electrodes is magnified by a low–noise amplifier (Stanford Research 560). The amplified voltage fluctuation signal is processed with a dynamic signal analyzer (Stanford Research 780) by converting the signal from the time domain to the frequency domain using a Fourier Transform. The applied voltage from the battery is divided among a potentiometer (100 Ω max), a load resistor (3.6 kΩ), R_L, and a device under test. The load resistor is selected with a value close to that of the device resistance. Using two voltage meters Vm_1 and Vm_2 , the total voltage drop across the load resistor and device are measured. The resistance across the device can then be calculated and the current spectra density can be derived as [23]:

$$S_I = S_V \left[\frac{(R_L+R_D)}{R_L R_D}\right]^2 \tag{5.6}$$

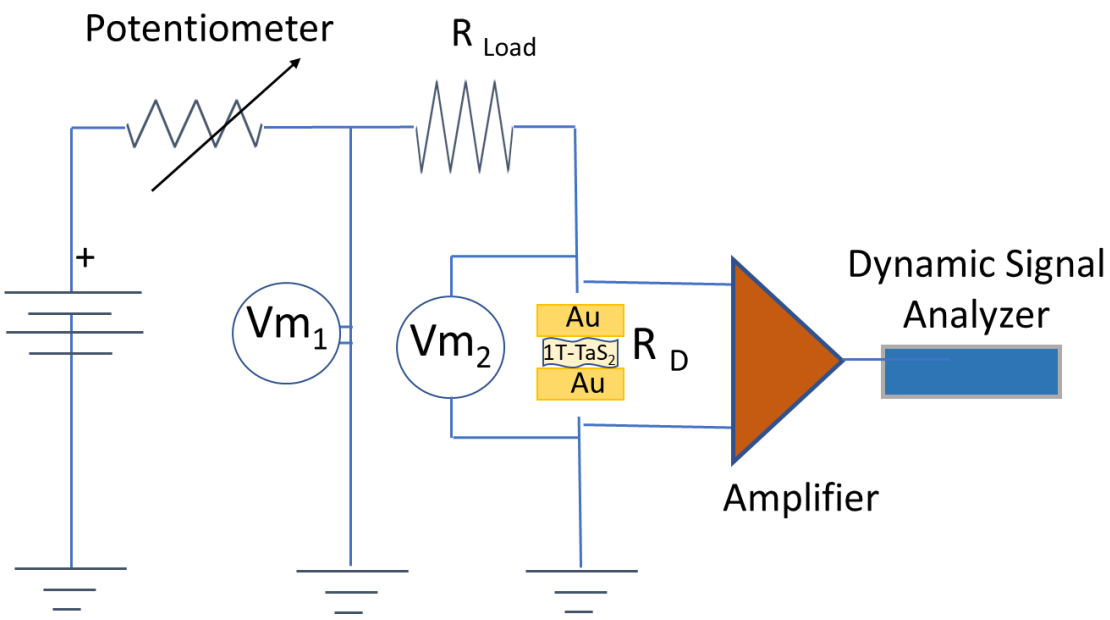

Figure 5.6: Schematic representation of a low – frequency noise measurement set – up.

5.7 References

[1] Brambley, D. R., "Electron–Beam Technology in Microelectronic Fabrication," *IEE Proc. I Solid State Electron Devices*, pp. 59–140 2010.

[2] Mohammad, M. A., Muhammad, M., Dew, S. K., and Stepanova, M., "Fundamentals of Electron Beam Exposure and Development," Springer Vienna, 2012.

[3] Sarangan, A., "Nanofabrication," in *Fundamentals and Applications of Nanophotonics*, pp. 149–184, 2016.

[4] Tseng, A. A., Chen, K., Chen, C. D., and Ma, K. J., "Electron Beam Lithography in Nanoscale Fabrication: Recent Development," *IEEE Trans. Electron. Packag. Manuf.*, vol. 26, pp. 141–149, 2003.

[5] Bajuri, S. N. M., Hamidah, N., Halim, A., and Kangar–arau, J., "PMMA Characterization and Optimization for Nano Structure Formation," *1st Natl. Conf. Electron. Des.*, pp. 81–83, 2005.

[6] Gammelgaard, L., Caridad, J. M., Cagliani, A., MacKenzie, D. M. A., Petersen, D. H., Booth, T. J., and Bøggild, P., "Graphene Transport Properties upon Exposure to PMMA Processing and Heat Treatments," *2D Mater.*, vol. 1, 035005, 2014.

[7] Kaleli, B., Aarnink, A. A. I., Smits, S., Hueting, R. J. E., Wolters, R. A. M., and Schmitz, J., "Electron Beam Lithography of HSQ and PMMA Resists and Importance of Their Properties to Link the Nano World to the Micro World," in *Proc. STW ICT Conf*, pp. 105–108, 2010.

[8] Carlberg, P., Graczyk, M., Sarwe, E. L., Maximov, I., Beck, M., and Montelius, L., "Lift–off Process for Nanoimprint Lithography," in *Microelectronic Engineering*, vol. 67, pp. 203–207, 2003.

[9] Yasin, S., Hasko, D. G., and Ahmed, H., “Comparison of MIBK/IPA and Water/IPA as PMMA Developers for Electron Beam Nanolithography,” in *Microelectronic Engineering*, vol. 61, pp. 745–753, 2002.

[10] Bishop, C. A., “Vacuum Deposition onto Webs, Films and Foils", Wiliam Andrew, 2012.

[11] Balzers High Vacuum Limited, UK, “Electron–Beam Evaporation,” *Vacuum*, vol. 15, 510, 2002.

[12] Frey, H., “Chemical Vapor Deposition (CVD),” in *Handbook of Thin–Film Technology*, pp. 225–252, 2015.

[13] Dobkin, D. M. and Zuraw, M. K., "Principles of Chemical Vapor Deposition.", Springer Netherlands, 2013.

[14] Deposition, C. V., “The Fundamentals of Chemical Vapour Deposition,” *J. Mater. Sci.*, vol. 12, pp. 1285–1306, 1977.

[15] Barin, G. B., Song, Y., Gimenez, I. D. F., Filho, A. G. S., Barreto, L. S., and Kong, J., “Optimized Graphene Transfer: Influence of Polymethylmethacrylate (PMMA) Layer Concentration and Baking Time on Grapheme Final Performance,” *Carbon*, vol. 84, pp. 82–90, 2015.

[16] Choi, J. Y., “Graphene Transfer: A Stamp for All Substrates,” *Nature Nanotechnology*., vol. 8, pp. 311–312, 2013.

[17] Nam, J., Lee, Y., Choi, W., Kim, C. S., Kim, H., Kim, J., Kim, D. H., and Jo, S., “Transfer Printed Flexible and Stretchable Thin Film Solar Cells Using a Water–Soluble Sacrificial Layer,” *Adv. Energy Mater.*, 1601269, 2016.

[18] Ren, Y., Zhu, C., Cai, W., Li, H., Hao, Y., Wu, Y., Chen, S., Wu, Q., Piner, R. D., and Ruoff, R. S.,“An Improved Method for Transferring Graphene Graphene Grown by Chemical Vapor Deposition," *Nano*, vol.7, 1150001, 2012.

[19] Smythe, E. J., Dickey, M. D., Whitesides, G. M., and Capasso, F., "A Technique to Transfer Metallic Nanoscale Patterns to Small and Non–Planar Surfaces," *ACS Nano*, vol.3, pp. 59–65, 2009.

[20] Tien, D. H., Park, J. Y., Kim, K. B., Lee, N., Choi, T., Kim, P., Taniguchi, T., Watanabe, K., and Seo, Y., "Study of Graphene–Based 2D–Heterostructure Device Fabricated by All–Dry Transfer Process," *ACS Appl. Mater. Interfaces*, vol. 8, pp.3072–3078, 2016.

[21] Stolyarov, M. A., Liu, G., Bloodgood, M. A., Aytan, E., Jiang, C., Samnakay, R., Salguero, T. T., Nika, D. L., Rumyantsev, S. L., Shur, M. S., Bozhilov, K. N., and Balandin, A. A., "Breakdown Current Density in: H –BN–Capped Quasi–1D $TaSe_3$ Metallic Nanowires: Prospects of Interconnect Applications," *Nanoscale*, vol. 8, pp. 15774–15782, 2016.

[22] Castellanos–Gomez, A., Buscema, M., Molenaar, R., Singh, V., Janssen, L., Van der Zant, H. S. J., and Steele, G. A., "Deterministic Transfer of Two – Dimensional Materials by All–Dry Viscoelastic Stamping," *2D Mater.*, vol. 1, 011002, 2014.

[23] Balandin, A. A., "Low – Frequency 1/f Noise in Graphene Devices," *Nat. Nanotechnol.*, vol. 8, pp. 549–555, 2013.

[24] Hooge, F. N., Kleinpenning, T. G. M., and Vandamme, L. K. J., "Experimental Studies on 1/f Noise," *Reports on Progress in Physics*. vol. 44, pp. 479–532, 1981.

[25] Koga, Sh.,"Electronic Noise and Fluctuations in Solids" Cambridge University Press., 1996.

[26] MacDonald, K. C. and Lindsay, R. B., "*Noise and Fluctuations: An Introduction*," *Phys. Today*, vol. 16, pp. 74–75, 1963.

[27] Johnson, J. B., "The Schottky Effect in Low – Frequency Circuits," *Phys. Rev.*, vol. 26, pp. 71–85, 1925.

[28] Flinn, I., "Extent of the 1/f Noise Spectrum," *Nature*, vol. 219, pp. 1356–1357, 1968.

Chapter 6

6 1*T* – TaS_2 Device Characterization

6.1 Vertical 1*T* – TaS_2 Device

Recently, the study of CDW materials and devices has undergone a true renaissance [1–6]. Despite the increasing attention on 1*T* – TaS_2, there have been very few reports on the out–of – plane transport properties of the material. We are aware of only two reports on the electrical conduction anisotropy of 1*T* – TaS_2; one focused on bulk properties [7] and the other on ultra–thin films [8]. The most recent observation of the vertical transport properties of 1*T* – TaS_2 was reported in study that examined the out – of – plane Nernst effect, which is sensitive to the out–of–plane electronic structure [1]. In this dissertation, we use low –frequency noise (LFN) spectroscopy as a tool to examine changes in the out–of – plane transport properties of 1*T* – TaS_2 as it undergoes CDW phase transitions via temperature stimuli.

High–quality 1*T* – TaS_2 crystals were prepared by the chemical vapor transport method. The prototype vertical devices were fabricated via mechanical exfoliation and an all dry transfer method. The device fabrication process can be briefly described in the following steps. First, bottom electrodes were patterned by electron beam lithography

(EBL) (LEO Supra) on a SiO_2/Si substrate. Immediately after, layers of Ti/Au metal were deposited by e–beam evaporation (Temescal BJD). Thin 1*T* – TaS_2 layers were exfoliated from bulk crystals onto an ultra – clean PDMS/glass stamp which was mounted onto a transfer stage equipped with a micromanipulator to align and transfer the exfoliated layers from the PDMS surface onto the bottom electrode. Thin layers of hexagonal Boron Nitride (h – BN) were then placed overlapping the edge of 1*T* – TaS_2 layers using the same dry – stamp transfer technique, to avoid any unwanted edge contacts. Finally, top electrodes consisting of Ti/Au metal were fabricated using EBL and e – beam evaporation. A schematic of the completed device structure is shown in Figure 6.1.

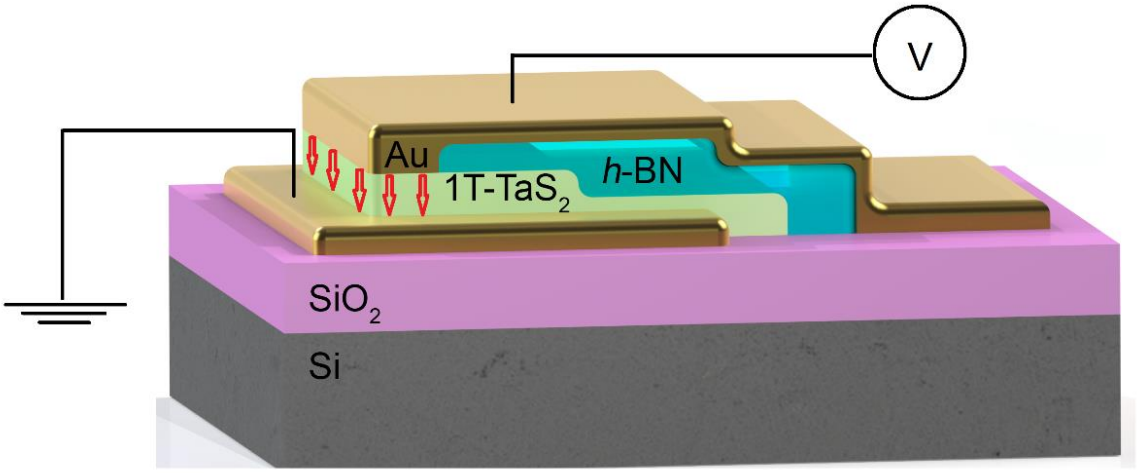

Figure 6.1: TaS_2 vertical device schematic. Reprinted with permission from R. Salgado, A. Mohammadzadeh, F. Kargar, A. Geremew, C. Huang, M. A. Bloodgood, S. Rumyantsev, T. T. Salguero, A. A. Balandin "Low – frequency noise spectroscopy of charge – density-wave phase transitions in vertical quasi – 2D 1*T* – TaS_2 devices," Appl. Phys. Express, vol. 12, 037001, 2019. Copyright © 2019 The Japan Society of Applied Physics.

6.2 Electrical Resistance Measurements

Temperature dependent current–voltage (I–V) characteristics were measured in a Lakeshore cryogenic probe station TTPX with a semiconductor analyzer Agilent B1500. To conduct temperature dependent measurement, the Lakeshore vacuumed chamber which houses the device is cooled down using liquid nitrogen. The temperature is controlled with an electrical heater in the chamber which is controlled using a Lakeshore 336 temperature controller module. In this configuration, the lakeshore probe is able to measure the electrical characteristics of devices from 77 K up to 400 K. Figure 6.2 a) shows the measured temperature dependent resistance of a two – terminal $1T - TaS_2$ vertical device. The insert images of Figure 6.2 a) shows the optical image of two typical $1T - TaS_2$ vertical devices. The cross – sectional area and thickness of the $1T - TaS_2$ layer were around 0.5 μm^2 and 90 nm, respectively. The vertical devices were cooled down to 78 K at a ramp down rate of 1.5 K/min and heated at the same rate back to room temperature. The tested devices reached temperature stability in between the heating and cooling cycle while their resistance was measured at a DC bias sweep from 0 to 10 mV. The observed resistance hysteresis curve corresponding to the commensurate and near–commensurate CDW phases is in line with previous reported studies [8].

An abrupt change in resistance can be observed below this transition temperature. Figure 6.2 b) shows the temperature dependent resistance of three different devices measured below their C – NC CDW phase transition temperature, measured during the

cooling cycle. The abrupt resistance drop can be seen in all measured devices below the expected phase transition which ranged from 80 K to 100 K

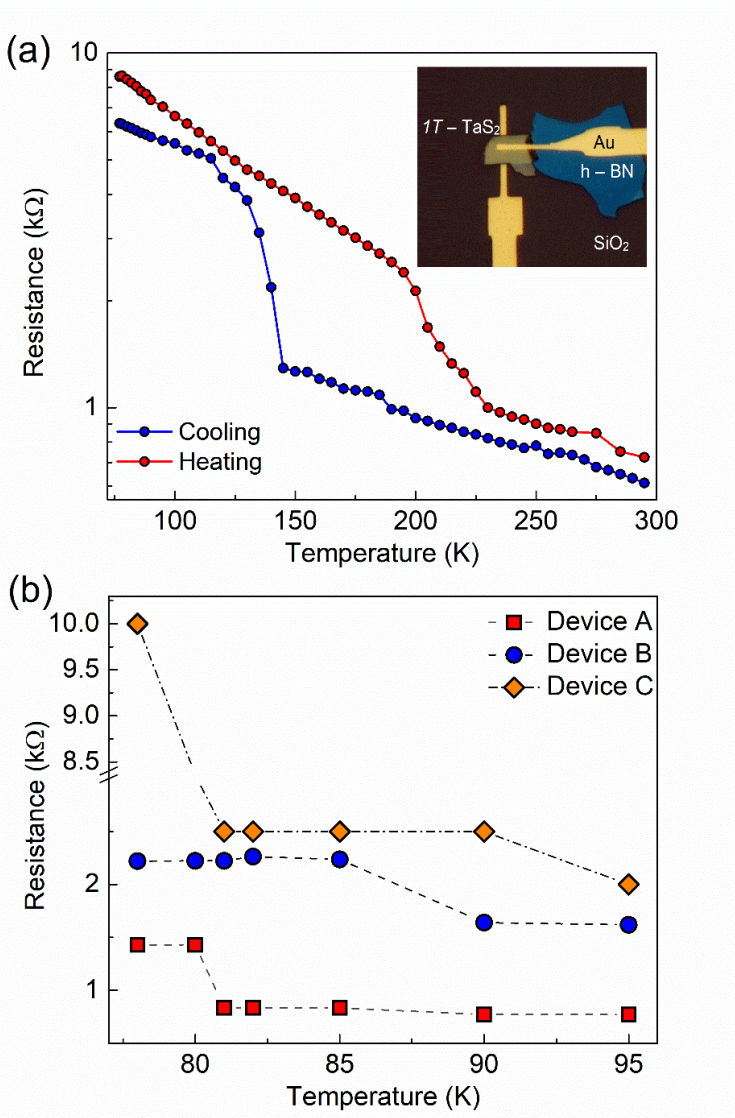

Figure 6.2: (a) Electrical resistance of a representative vertical 1*T* – TaS_2 device measured in the cooling and heating cycles. The insert shows an annotated optical microscopy image of the vertical device. (b) Electrical resistance of three different vertical 1*T* – TaS_2 devices measured below the well-known commensurate to nearly – commensurate charge – density – wave transition temperature. Reprinted with permission from R. Salgado, A. Mohammadzadeh, F. Kargar, A. Geremew, C. Huang, M. A. Bloodgood, S. Rumyantsev, T. T. Salguero, A. A. Balandin "Low – frequency noise spectroscopy of charge – density – wave phase transitions in vertical quasi – 2D 1*T* – TaS_2 devices," Appl. Phys. Express, vol. 12, 037001, 2019. Copyright © 2019 The Japan Society of Applied Physics.

6.3 Low – Frequency Noise Measurements

LFN spectroscopy measurements were taken to examine these unusual resistance changes using a custom – built experimental setup with a spectrum analyzer (SRS FFT). The devices were DC biased with a "quiet" battery – potentiometer circuit, to minimize the 60 Hz noise peak and its harmonics. A source–drain bias was applied to the vertical device via a biasing circuit consisting of a single rechargeable 6 V lead acid battery. The device bias ranges from 0 V to 80 mV. Multi–turnable 2 W potentiometers are used to tune the applied biases, 100 Ω in the source–drain biasing circuit and 3.6 kΩ in the biasing circuit. More details of our low–noise measurement procedure can be found elsewhere [9–13]. Figure 6.3 a) shows the room temperature noise spectra of voltage fluctuations, S_v, as a function of frequency for a typical 1*T*–TaS_2 vertical device under DC bias voltage, V_b, from 0.6 mV to 80 mV. The spectra follow the *1/f* behavior without any signatures of generation–recombination bulges.

We calculated the short–circuit current fluctuations following the conventional formula as $S_I=S_v[(R_L+R_D)/(R_LR_D)]^2$, where R_L and R_D are the load and device resistances, respectively. Figure 6.3 b) shows noise density as a function of current which demonstrates perfect scaling with I^2 which is expected for conventional *1/f* noise behavior. This proportionality implies that current does not drive the fluctuations but merely accentuates their visibility following Ohm's law.

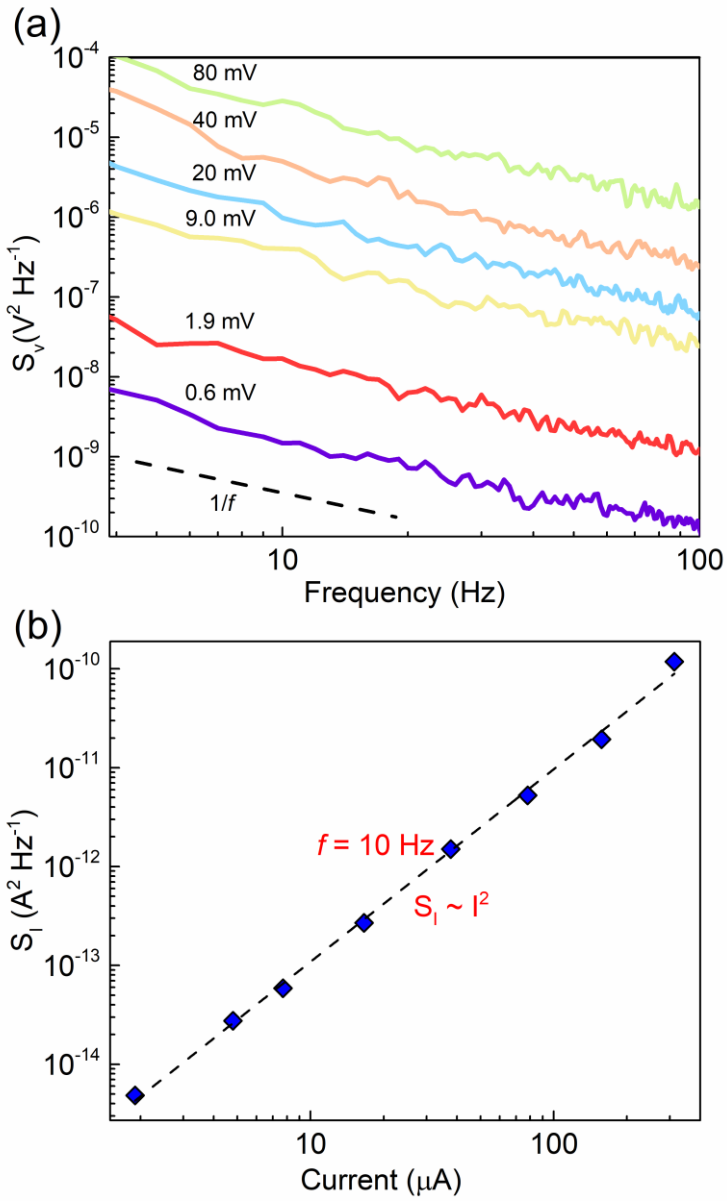

Figure 6.3: (a) Low – frequency current noise spectral density as a function of frequency for a vertical 1*T* – TaS_2 charge – density – wave device. The room – temperature data are shown for the bias voltage ranging from 0.6 mV to 80 mV. Note that all noise spectra are of the 1/f type without any signatures of the Lorentzian bulges. (b) Noise spectral density as a function of the electric current between two device terminals at a fixed frequency f=10 Hz. Reprinted with permission from R. Salgado, A. Mohammadzadeh, F. Kargar, A. Geremew, C. Huang, M. A. Bloodgood, S. Rumyantsev, T. T. Salguero, A. A. Balandin "Low – frequency noise spectroscopy of charge–density–wave phase transitions in vertical quasi – 2D 1*T* – TaS_2 devices," Appl. Phys. Express, vol. 12, 037001, 2019. Copyright © 2019 The Japan Society of Applied Physics.

We performed low temperature LFN and electrical resistance measurements on a vertical 1*T* – TaS_2 device as it was heated from 77 K to above the C – NC CDW phase transition temperature. In Figure 6.4, we show the measured electrical resistance, at a voltage sweep of 10 mV, and the evolution of the normalized current noise, S_I/I^2, with temperature, at a Vb = 13 mV and frequency of 10 Hz. The sudden drop in resistance observed around 160 K is in agreement with what has been observed as the C – NC CDW phase transition temperature. The peak in the normalized current noise spectrum around 160 K corresponds to this phase transition. The unusual drop in resistance seen in previous vertical 1*T* – TaS_2 devices below the C – NC phase transition temperature can be observed around 100K and is accompanied by a peak in the normalized current fluctuation spectrum.

We previously reported low – frequency noise measurements on planar 1*T* – TaS_2 devices and discovered that the noise in 2D CDW systems has a unique physical origin correlated to the evolution and interaction of large discrete fluctuators [10]. The assumption was that these fluctuators were associated with groups of C – CDW domains and islands, commensurate regions of the NC – C CDW phase, and the material system switching in between phases. The electrical noise in these devices had two pronounced maxima which corresponded to the onset of CDW sliding and the NC – IC CDW phase transition brought upon by electrical stimuli. Our results proved that LFN spectroscopy can be a powerful tool in uncovering transport phenomena in mixed phases. Since many CDW materials can undergo a phase transition, these results are important to advance the understanding of governing principles of CDW and future device paradigms.

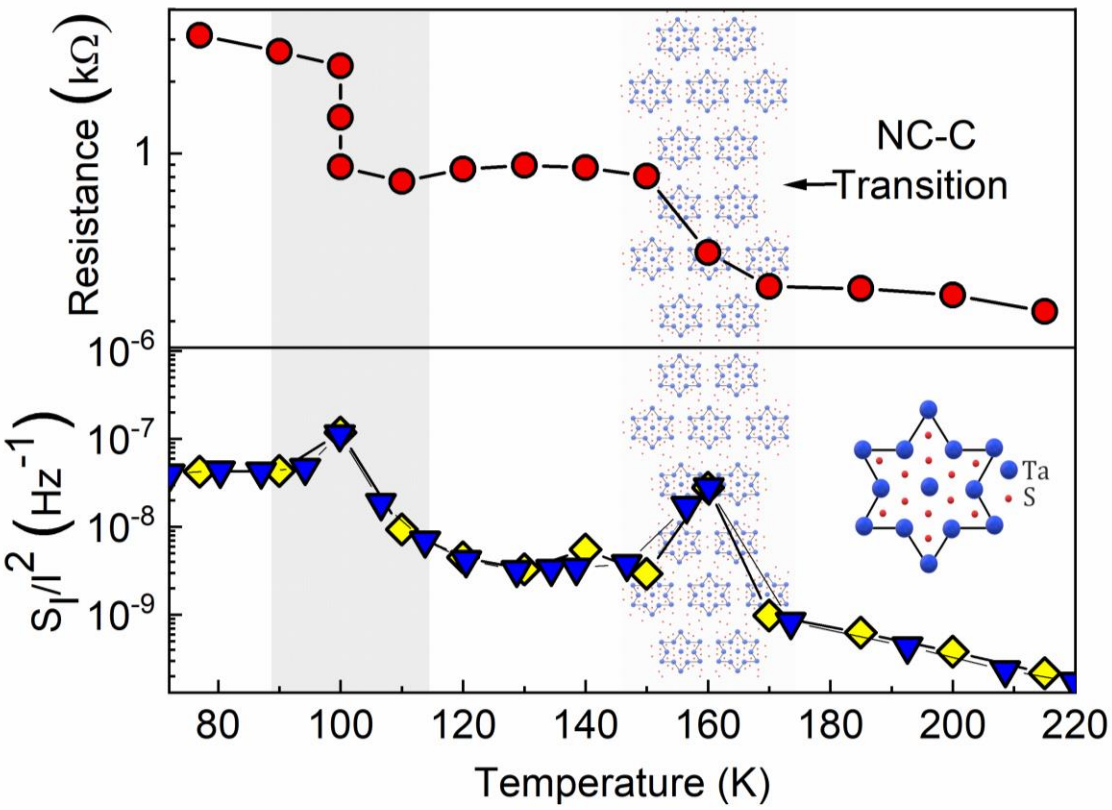

.

Figure 6.4: Low temperature LFN measurements from room temperature down to 77 K, at V_{ds} =13 mv bias. The evolution of the normalized current noise with temperature, at a frequency of 10 Hz, can be seen. Reprinted with permission from R. Salgado, A. Mohammadzadeh, F. Kargar, A. Geremew, C. Huang, M. A. Bloodgood, S. Rumyantsev, T. T. Salguero, A. A. Balandin "Low – frequency noise spectroscopy of charge – density – wave phase transitions in vertical quasi – 2D 1*T* – TaS_2 devices," Appl. Phys. Express, vol. 12, 037001, 2019. Copyright © 2019 The Japan Society of Applied Physics.

It is important to note that the noise spectra measured at temperatures far from the phase transition temperature are always of the 1/*f* type, as seen in previous work [10]. The electronic noise spectra within the noise peak, which corresponds to the phase transition, have the shape of the well – defined Lorentzian form. Figure 6.5 shows the noise spectra

at 98 K, which corresponds to a so called hidden phase transition, in the vertical device configuration.

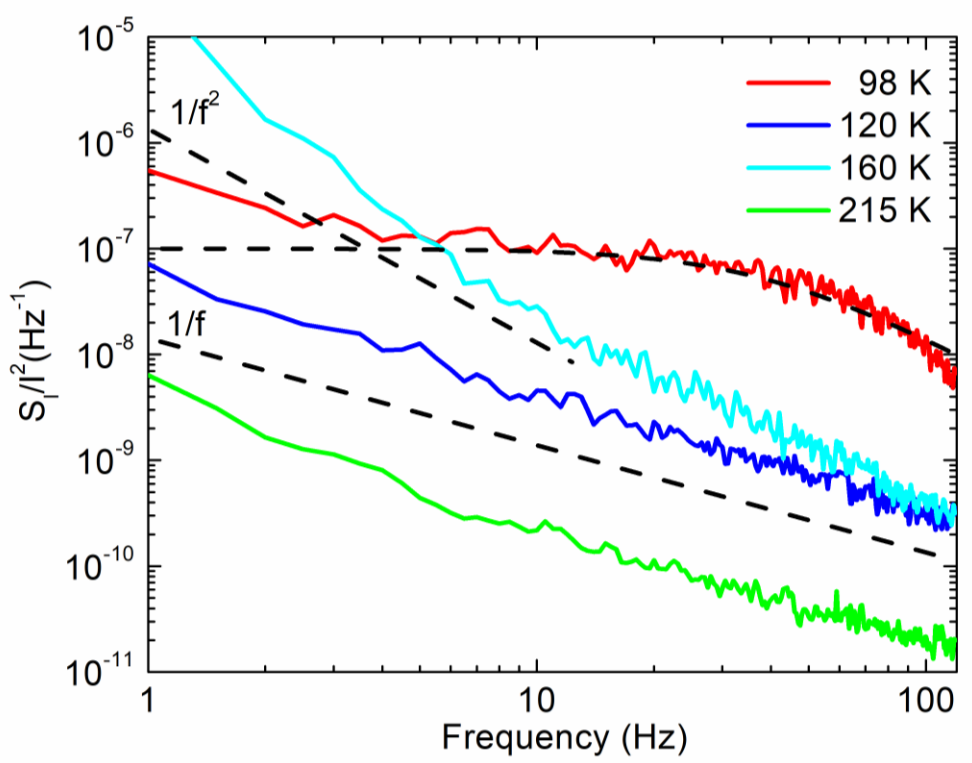

Figure 6.5: Current normalized noise spectra at different temperatures. Reprinted with permission from R. Salgado, A. Mohammadzadeh F. Kargar A. Geremew, C. Huang, M. A. Bloodgood, S. Rumyantsev, T. T. Salguero, A. A. Balandin "Low – frequency noise spectroscopy of charge – density – wave phase transitions in vertical quasi – 2D 1*T* – TaS_2 devices," Appl. Phys. Express, vol. 12, 037001, 2019. Copyright © 2019 The Japan Society of Applied Physics.

At a frequency of 8 Hz, the noise spectrum at 98 K is close to the Lorentzian form as shown by the dashed curve, described as $S_I/I^2 \sim A/[1+(2\pi f\tau)^2]$, where A is a constant and $\tau \sim 4\times10^{-3}$ s is a time constant, which characterizes the dynamics of the phase

transition. The characteristic time τ of the Lorentzian spectra corresponds to the specifics of the transition and applied voltage. The noise spectrum at 160 K corresponds to the known C – NC CDW phase transition and reveals a characteristic Lorentzian frequency below 1 Hz, only the tail of the $1/f^2$ part of the spectrum is visible. It is interesting to note that the noise spectra measured the same temperature in planar 1*T* – TaS_2 devices do not show any signs of a Lorentzian shape. This suggests that the Lorentzian spectra demonstrated in the vertical device configuration is not a result of a generation–recombination process but an actual phase transition. The sharp increase in noise near and at the phase transition is well–known for other materials [14,15]. It can also be associated with abrupt changes in resistance and instability characteristics of the material during the phase transition.

6.4 Summary

We have described the cross – plane electron transport in vertical quasi–2D layered 1*T* – TaS_2 CDW devices using low – frequency noise spectroscopy to study changes in the electrical characteristics below RT. We observed two steps in electrical resistivity in the temperature range from 150 K to 180 K, and in the range from 80 K to 85 K. The normalized low – frequency noise spectral density revealed strong peaks at these transition points, changing by more than an order–of–magnitude. The higher temperature feature was associated with the well–known transition between the C – CDW and NC – CDW states. The lower temperature transition may indicate the presence of the “hidden” CDW phase.

These results further support the potential of the low – frequency noise spectroscopy for investigating electron transport in vertically – stacked quasi – 2D materials.

6.5 References

[1] Wu, S. M., Luican–Mayer, A., and Bhattacharya, A., "Nanoscale Measurement of Nernst Effect in Two – Dimensional Charge Density Wave Material 1T–TaS_2," *Appl. Phys. Lett.*, vol. 111, 223109, 2017.

[2] Stojchevska, L., Vaskivskyi, I., Mertelj, T., Kusar, P., Svetin, D., Brazovskii, S., and Mihailovic, D., "Ultrafast Switching to a Stable Hidden Topologically Protected Quantum State in an Electronic Crystal," *Science.*, vol. 344, pp. 177–80, 2014.

[3] Sipos, B., Kusmartseva, A. F., Akrap, A., Berger, H., Forró, L., and Tutǐ, E., "From Mott State to Superconductivity in 1T–TaS_2," *Nat. Mater.*, vol. 7, pp. 960–965, 2008.

[4] Samnakay, R., Wickramaratne, D., Pope, T. R., Lake, R. K., Salguero, T. T., and Balandin, A. A., "Zone–Folded Phonons and the Commensurate–Incommensurate Charge–Density–Wave Transition in 1 T –$TaSe_2$ Thin Films," *Nano Lett.*, vol. 15, pp. 2965–2973, 2015.

[5] Rossnagel, K., "On the Origin of Charge–Density Waves in Select Layered Transition–Metal Dichalcogenides," *Journal of Physics Condensed Matter*. vol. 23, 213001, 2011.

[6] Porer, M., Leierseder, U., Ménard, J. M., Dachraoui, H., Mouchliadis, L., Perakis, I. E., Heinzmann, U., Demsar, J., Rossnagel, K., and Huber, R., "Non–Thermal Separation of Electronic and Structural Orders in a Persisting Charge Density Wave," *Nat. Mater.*, vol. 13, pp. 857–861, 2014.

[7] Hambourger, P. D. and di Salvo, F. J., "Electronic Conduction Process in 1T–TaS_2," *Phys. B+C*, vol. 99, pp. 173–176, 1980.

[8] Svetin, D., Vaskivskyi, I., Brazovskii, S., and Mihailovic, D., "Three – Dimensional Resistivity and Switching between Correlated Electronic States in 1T–TaS_2," *Sci. Rep.*, vol. 7, 46048, 2017.

[9] Liu, G., Stillman, W., Rumyantsev, S., Shao, Q., Shur, M., and Balandin, A. A., "Low – Frequency Electronic Noise in the Double–Gate Single–Layer Graphene Transistors," *Appl. Phys. Lett.*, vol. 95, 033103, 2009.

[10] Liu, G., Rumyantsev, S., Bloodgood, M. A., Salguero, T. T., and Balandin, A. A., "Low – Frequency Current Fluctuations and Sliding of the Charge Density Waves in Two – Dimensional Materials," *Nano Lett.*, vol. 18, pp. 3630–3636, 2018.

[11] Liu, G., Rumyantsev, S., Shur, M. S., and Balandin, A. A., "Origin of 1/f Noise in Graphene Multilayers: Surface vs. Volume," *Appl. Phys. Lett.*, vol. 102, 093111, 2013.

[12] Renteria, J., Samnakay, R., Rumyantsev, S. L., Jiang, C., Goli, P., Shur, M. S., and Balandin, A. A., "Low – Frequency 1/f Noise in MoS_2 Transistors: Relative Contributions of the Channel and Contacts," *Appl. Phys. Lett.*, vol. 104, 153104, 2014.

[13] Rumyantsev, S., Liu, G., Stillman, W., Shur, M., and Balandin, A. A., "Electrical and Noise Characteristics of Graphene Field–Effect Transistors: Ambient Effects, Noise Sources and Physical Mechanisms," *J. Phys. Condens. Matter*, vol. 22, 395302, 2010.

[14] Kundu, H. K., Ray, S., Dolui, K., Bagwe, V., Choudhury, P. R., Krupanidhi, S. B., Das, T., Raychaudhuri, P., and Bid, A., "Quantum Phase Transition in Few–Layer $NbSe_2$ Probed through Quantized Conductance Fluctuations," *Phys. Rev. Lett.*, vol. 119, 226802, 2017.

[15] Kawasaki, M., Chaudhari, P., and Gupta, A., "1/f Noise in $YBa_2Cu_3O_{7-\zeta}$ Superconducting Bicrystal Grain–Boundary Junctions," *Phys. Rev. Lett.*, vol. 68, pp. 1065–1068, 1992.